

The UK Infrared Telescope M 33 monitoring project. V. The star formation history across the galactic disc

Atefeh Javadi¹, Jacco Th. van Loon², Habib G. Khosroshahi¹,
Fatemeh Tabatabaei^{3,4}, Roya Hamedani Golshan^{1,5} and Maryam Rashidi⁶

¹*School of Astronomy, Institute for Research in Fundamental Sciences (IPM), P.O. Box 19395-5531, Tehran, Iran*

²*Lennard-Jones Laboratories, Keele University, ST5 5BG, UK*

³*Instituto de Astrofísica de Canarias, Vía Láctea S/N, E-38205 La Laguna, Spain*

⁴*Departamento de Astrofísica, Universidad de La Laguna, E-38206 La Laguna, Spain*

⁵*Department of Physics, Faculty of Science, University of Isfahan, Isfahan, P.O. Box 81746-73441, Iran*

⁶*Physics Department, Alzahra University, Vanak, 1993891176, Tehran, Iran*

Submitted: 2016

ABSTRACT

We have conducted a near-infrared monitoring campaign at the UK InfraRed Telescope (UKIRT), of the Local Group spiral galaxy M 33 (Triangulum). On the basis of their variability, we have identified stars in the very final stage of their evolution, and for which the luminosity is more directly related to the birth mass than the more numerous less-evolved giant stars that continue to increase in luminosity. In this fifth paper of the series, we construct the birth mass function and hence derive the star formation history across the galactic disc of M 33. The star formation rate has varied between $\sim 0.010 \pm 0.001$ ($\sim 0.012 \pm 0.007$) and 0.060 ± 0.005 (0.052 ± 0.009) $M_{\odot} \text{ yr}^{-1} \text{ kpc}^{-2}$ statistically (systematically) in the central square kiloparsec of M 33, comparable with the values derived previously with another camera. The total star formation rate in M 33 within a galactocentric radius of 14 kpc has varied between $\sim 0.110 \pm 0.005$ ($\sim 0.174 \pm 0.060$) and $\sim 0.560 \pm 0.028$ ($\sim 0.503 \pm 0.100$) $M_{\odot} \text{ yr}^{-1}$ statistically (systematically). We find evidence of two epochs during which the star formation rate was enhanced by a factor of a few – one that started ~ 6 Gyr ago and lasted ~ 3 Gyr and produced $\geq 71\%$ of the total mass in stars, and one ~ 250 Myr ago that lasted ~ 200 Myr and formed $\leq 13\%$ of the mass in stars. Radial star formation history profiles suggest that the inner disc of M 33 was formed in an inside-out formation scenario. The outskirts of the disc are dominated by the old population, which may be the result of dynamical effects over many Gyr. We find correspondence to spiral structure for all stars, but enhanced only for stars younger than ~ 100 Myr; this suggests that the spiral arms are transient features and not part of a global density wave potential.

Key words: stars: luminosity function, mass function – galaxies: evolution – galaxies: individual: M 33 – galaxies: spiral – galaxies: stellar content – galaxies: structure

1 INTRODUCTION

Galactic evolution is driven at the end-points of stellar evolution, where copious mass loss returns chemically-enriched and sometimes dusty matter back to the interstellar medium (ISM); the stellar winds of evolved stars and the violent deaths of the most massive stars also inject energy and momentum into the ISM, generating turbulence and galactic fountains when superbubbles pop as they reach the “surface” of the galactic disc. Evolved stars are also excellent tracers, not just of the feedback processes, but also of the underlying populations, that were formed from millions to billions of years prior to their appearance. The evolved phases

of evolution generally represent the most luminous, and often the coolest, making evolved stars brilliant beacons at IR wavelengths, where it is also easier to see them deep inside galaxies as dust is more transparent at those longer wavelengths than in the optical and ultraviolet where their progenitors shine. The final stages of evolution of stars with birth masses up to $M \sim 30 M_{\odot}$ – Asymptotic Giant Branch (AGB) stars and red supergiants (RSGs) – are characterised by strong radial pulsations of the cool atmospheric layers, rendering them identifiable as long-period variables (LPVs) in photometric monitoring campaigns spanning months to years (e.g., Whitelock, Feast & Catchpole 1991; Wood et al. 1992; Wood 2000; Ita et al. 2004a,b).

The prevalent theory of disc galaxy formation hinges on the formation of isolated discs through the dissipational collapse of a gaseous proto-galaxy embedded in cold dark matter halos (White & Rees 1978; Fall & Efstathiou 1980; Peebles 1984). Thin discs are built through gas accretion, while spheroids and thick discs are built via mergers (Steinmetz & Navarro 2002; Brook et al. 2004; Brooks et al. 2009). An alternative scenario for disc formation is based on gas-rich major mergers (Robertson et al. 2006; Stewart et al. 2009). In fact, each of these scenarios may operate depending on galaxy environments (Blanton et al. 2003). Spatially-resolved observational estimates of the star formation histories (SFHs) – and stellar chemical abundances – in spiral galaxies are a robust way to constrain models for their formation and evolution (Eggen et al. 1962; Freeman & Bland-Hawthorn 2002). This has become possible within galaxies of the Local Group (e.g., Sarajedini et al. 2000; Harbeck et al. 2001; Ferguson et al. 2002; Brown et al. 2003; Cole et al. 2005). All those methods rely on theoretical models of stellar evolution to provide stellar ages and evolutionary lifetimes, as well as stellar yields, and an assumption about the initial mass function (IMF) at which stars are born.

M33 is a low luminosity, late type disc spiral galaxy in the Local Group of galaxies. With a stellar mass of $M_* \sim 3\text{--}6 \times 10^9 M_\odot$ and neutral gas mass of $M_{\text{gas}} \sim 3 \times 10^9 M_\odot$ (Corbelli 2003), M33 is less massive but more gas-rich than the Milky Way disc, which has $M_* \sim 5 \times 10^{10} M_\odot$ (Licquia & Newman; cf. McMillan 2011) and $M_{\text{gas}} \sim 1 \times 10^{10} M_\odot$ (Nakanishi & Sofue 2015), with no sign of recent mergers. In addition to its proximity (distance modulus $\mu = 24.9$ mag; Bonanos et al. 2006; U et al. 2009), its large – but not too large – angular size ($\sim 1^\circ$) and low inclination (56°) offer us a unique opportunity to study its stellar populations, their history and their feedback across an entire spiral galaxy. Using colour–magnitude diagrams (CMDs) of resolved stars in M33, Barker et al. (2007) found a positive age gradient in three fields just outside the break radius on the southern minor axis. More recently, Williams et al. (2009) found a negative age gradient within the break radius in the radial mass profile, $r < 6$ kpc, in four fields on M33s southern major axis. This hints at multiple mechanisms at play, that shaped the M33 disc as we see it today, and calls for independent, homogeneous analyses across the entire span of the M33 galaxy. Here we provide such study.

The main objectives of our project are described in Javadi, van Loon & Mirtorabi (2011c): to construct the mass function of LPVs and derive from this the SFH in M33; to correlate spatial distributions of the LPVs of different mass with galactic structures (spheroid, disc and spiral arm components); to measure the rate at which dust is produced and fed into the ISM; to establish correlations between the dust production rate, luminosity, and amplitude of an LPV; and to compare the *in situ* dust replenishment with the amount of pre-existing dust. Paper I in the series presented the photometric catalogue of stars in the inner square kpc (Javadi et al. 2011a), with Paper II presenting the galactic structure and SFH (Javadi, van Loon and Mirtorabi 2011b), and Paper III presenting the mass-loss mechanism and dust production rate (Javadi et al. 2013). Paper IV presented the photometric catalogue of stars in a nearly square degree area covering much of the M33 optical disc. This fifth paper in the series covers the SFH across the enlarged area; the next

paper will present an analysis of the mass return to the M33 disc.

2 INPUT DATA AND MODELS

2.1 Catalogue of variable stars

In paper IV we described the method employed to identify large-amplitude LPVs across the galactic disc of M33 with the WFCAM imager on the United Kingdom IR Telescope (UKIRT) on Mauna Kea, Hawai'i. The area that was monitored covers almost a square degree ($53' \times 53'$); given the inclination and distance of M33, we thus probe all of its disc out to a galactocentric radius of 7.5 kpc, i.e. $0.88 R_{25}$ (optical radius), and out to 15 kpc ($1.76 R_{25}$) in certain directions. The observations were done between 2005–2007 in the K_s -band ($\lambda = 2.2 \mu\text{m}$) with occasionally observations in J- and H-bands ($\lambda = 1.28$ and $1.68 \mu\text{m}$, respectively) for the purpose of obtaining colour information.

The photometric catalogue comprises 403 734 stars, among which 4643 stars were identified as LPVs – AGB stars, super-AGB stars and RSGs. Their distribution over magnitude and colour is shown in Fig. 1. Some brighter variable RSGs are found (around $K_s \sim 14$ mag), but the clump of variable stars with $K_s < 11$ mag are foreground stars and all are saturated. These stars are removed from further analysis. The amplitude is generally $A_K \leq 1$ mag, but a small fraction of variable stars (8%) reach $A_K > 2$ mag. Among these extreme variables, 311 have six or fewer measurements and their amplitudes are therefore unreliable. Disregarding those, only 20 stars remain with $A_K > 3$ mag.

We separate the stars in our catalogue into three categories: massive stars, AGB stars and RGB stars, on the basis of K_s -band magnitude and $(J - K_s)$ colour criteria (see Fig. 1). We define a demarcation line between hot massive stars and cooler, less-massive giant stars to run from $(J - K_s, K_s) = (0.6, 18)$ to $(J - K_s, K_s) = (0.9, 15.6)$ mag, with massive stars those that have $(J - K_s)$ colours bluer than this (down to $K_s = 19.5$ mag) or that have $K_s < 15.6$ mag, and AGB stars and RGB stars those that have $(J - K_s)$ colours redder than this and that have $16 < K_s < 18$ mag (AGB) or $18.3 < K_s < 19.5$ mag (RGB, which does extend to much fainter magnitudes than our survey completeness). We left small gaps to avoid contamination. The distributions of different types of near-IR populations across the galactic disc of M33 is shown in Fig. 2, deprojected onto the M33 galactic plane, with dashed lines showing the distributions for the variables that were identified in our near-IR monitoring programme. There is a clear difference between the stellar populations within the inner $r < 1$ kpc, with RGB stars showing a core but massive stars – in particular those identified by their variability – showing a cusp. Further out, all populations show a distribution consistent with an exponential disc. An exponential profile fit of the form $I = I_0 \exp(-r/r_0)$ yields $r_0 = 2.3$ for the AGB stars ($r_0 = 2.6$ kpc for the variables) and $r_0 = 2.6$ kpc for the massive stars ($r_0 = 3.4$ kpc for the variables, with a Sersic core). The RGB population, dominated by old stars, is fit with a Sersic profile, with $r_0 = 5$ kpc. This inflated distribution could be a sign of dynamical relaxation. The relatively large scalelength of the massive stars, which still reflect their

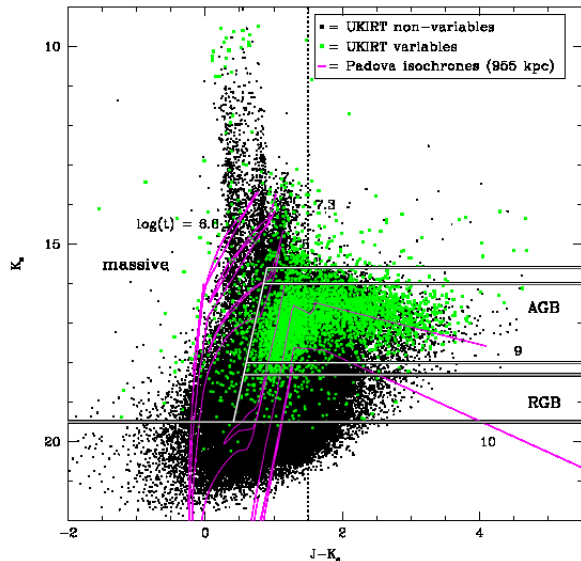


Figure 1. K_s versus $(J - K_s)$, with WFCAM variable stars in green. Overplotted are isochrones from Marigo et al. (2008) for solar metallicity and a distance modulus of $\mu = 24.9$ mag, labelled by their logarithmic ages – these include circumstellar reddening, showing up as large excursions towards red colours; carbonaceous dust (e.g., at $\log t = 9$) and oxygenous dust (e.g., at $\log t = 10$) have different reddening slopes. The vertical dashed line at $(J - K_s) = 1.5$ mag indicates the colour criterion redwards of which a correction is applied for this reddening. The thick black-and-white lines demarcate the bulk of the populations of massive, AGB and RGB stars (separated by small buffers in K -band magnitude to avoid cross-contamination).

birth sites, compared to the AGB stars may be an indication of the inside-out formation of the disc of M33, whilst the central hike in density of the massive stars may indicate accretion-induced star formation (see Paper II).

2.2 Stellar evolution models

The method used here to derive the SFH strongly depends on the AGB phase of stellar evolution. To date, the Padova models (Marigo et al. 2008) are the most realistic. The full AGB evolution is calculated – except for the super-AGB phase of stellar evolution ($M_{\text{birth}} \sim 6\text{--}9 M_{\odot}$; Siess 2007; Doherty et al. 2015), which is too fast to be calculated without a separate treatment. It accurately accounts for the third dredge-up, and hot bottom burning (HBB; Iben & Renzini 1983) in the most massive AGB stars ($M_{\text{birth}} \sim 4\text{--}6 M_{\odot}$). They also include the effects of molecular opacities in the cool stellar mantles and atmospheres, which

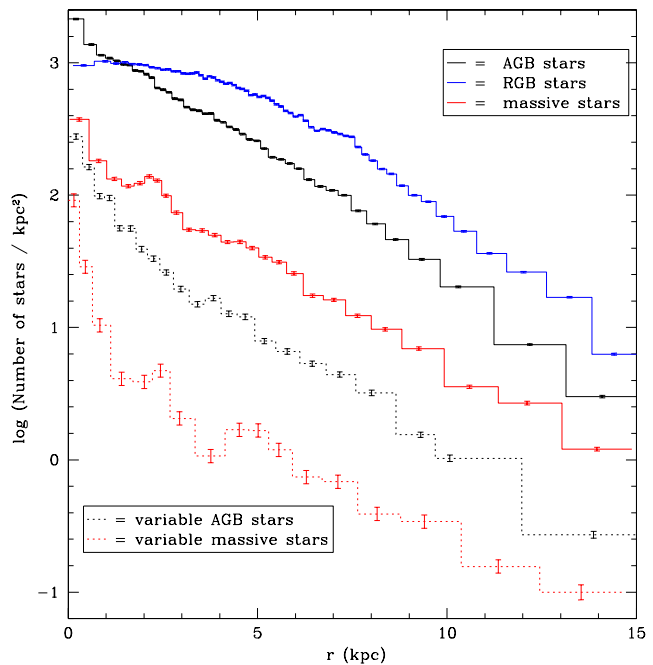


Figure 2. Radial distributions across a large part of M33 of the near-IR populations of cool evolved stars, deprojected onto the M33 galactic plane. Dashed lines are for the variable stars.

becomes especially apparent in the transformation from oxygen-dominated (M-type) AGB stars to carbon stars in the birth mass range $M_{\text{birth}} \sim 1.5\text{--}4 M_{\odot}$ (Girardi & Marigo 2007). In addition, and crucial for our method, the Padova models predict the pulsation properties and the effects of circumstellar dust production on the spectral energy distribution (SED) of the star plus its dust envelope. Separate models cover the massive stars, of which the lower mass range ($M_{\text{birth}} \sim 9\text{--}30 M_{\odot}$ become RSGs. The full suite of models thus enables us to evaluate the SFH from as long ago as 10 Gyr, to as recent as ~ 10 Myr ago.

That said, those models do not consider the effects of magnetic fields or rotation on the mixing process inside the stars. Including more efficient mixing would make stars live longer and massive stars evolve to cooler RSGs (Meynet & Maeder 2000; Heger, Woosley & Spruit 2005). Likewise, the life times of intermediate-mass stars are prolonged in the presence of convective overshoot (Marigo & Girardi 2007). Also, the thermal pulsing AGB is computed by adopting parameterisations for the efficiency of third dredge-up, and the threshold temperature at which it sets in, not by solving the equations governing the stellar internal structure.

3 METHODOLOGY: DERIVING THE SFH

In paper II, we presented a novel way to derive the SFH by using cool, large-amplitude LPVs which are identified in IR monitoring programmes. We use the fact that these variables have reached the very final stages of their evolution, and their brightness can thus be transformed into their mass at birth by employing theoretical evolutionary tracks, or by isochrones. The LPVs are located at the cool end of each of the isochrones. Hence, we convert the observed K -band magnitude (which is close to the peak in the SED, thus

minimising uncertainties in the bolometric corrections) into the birth mass.

This was done in paper II for four different metallicities, from super-solar – suitable for massive elliptical galaxies and stellar populations in the bulges of massive spiral galaxies such as the Milky Way – to sub-solar values appropriate for galaxies such as the Magellanic Clouds (Rezaeikh et al. 2014). As discussed in paper II, the central region of M 33 has an approximately solar metallicity (Rosolowsky & Simon 2008; Magrini et al. 2009), for which we adopt $Z = 0.015$. The disc of M 33 outside that central region is characterised by sub-solar metallicity; in paper IV we showed that $Z = 0.008$ agrees well with our CMDs as well as the literature. Magrini et al. (2007) derived an oxygen abundance gradient based on H II regions of -0.19 dex kpc^{-1} for $r < 3$ kpc and -0.038 dex kpc^{-1} for $r \geq 3$ kpc, suggesting a possibly slightly larger range of metallicities. However, in Paper II we showed that the SFHs derived using $Z = 0.0008$ and $Z = 0.015$ are very similar and hence we are not worried about small deviations from these typical values.

Since the method was described in detail in paper II, here we only provide a brief summary. The total mass of the stars created between times t and $t + dt$ is defined as:

$$dM(t) = \xi(t) dt, \quad (1)$$

where $\xi(t)$ is the star formation rate (SFR), in $M_\odot \text{ yr}^{-1}$. The mass $M(t)$ corresponds to the number of stars formed, N , as:

$$dN(t) = dM(t) \frac{\int_{\min}^{\max} f_{\text{IMF}}(m) dm}{\int_{\min}^{\max} f_{\text{IMF}}(m) m dm}, \quad (2)$$

where f_{IMF} is the IMF, which is described by:

$$f_{\text{IMF}} = A m^{-\alpha}, \quad (3)$$

where A is the normalisation factor and α is defined for different ranges in stellar mass, m , by Kroupa (2001):

$$\alpha = \begin{cases} +0.3 \pm 0.7 & \text{for } \min \leq m/M_\odot < 0.08 \\ +1.3 \pm 0.5 & \text{for } 0.08 \leq m/M_\odot < 0.50 \\ +2.3 \pm 0.3 & \text{for } 0.50 \leq m/M_\odot < \max \end{cases} \quad (4)$$

For the minimum and maximum of the stellar mass ranges we adopt $\min = 0.02 M_\odot$ and $\max = 200 M_\odot$, respectively.

The question now is how many of these stars, n , are LPVs around time t , which is when we observe them. The number of stars with mass between $m(t)$ and $m(t + dt)$ that were created between times t and $t + dt$ is:

$$dn(t) = dN(t) \frac{\int_{m(t)}^{m(t+dt)} f_{\text{IMF}}(m) dm}{\int_{\min}^{\max} f_{\text{IMF}}(m) dm}. \quad (5)$$

Combining the above equations we have:

$$dn(t) = \xi(t) dt \frac{\int_{m(t)}^{m(t+dt)} f_{\text{IMF}}(m) dm}{\int_{\min}^{\max} f_{\text{IMF}}(m) m dm}. \quad (6)$$

When we determine $\xi(t)$ over an age bin dt , the number of LPVs observed in that age bin, dn' , depends on the duration of the evolutionary phase of large-amplitude, long-period variability, the “pulsation duration” δt :

$$dn'(t) = dn(t) \frac{\delta t}{dt}. \quad (7)$$

Inverting the above equations, we obtain a relation between

the observed number of LPVs in a certain age bin, and the SFR that long ago:

$$\xi(t) = \frac{dn'(t)}{\delta t} \frac{\int_{\min}^{\max} f_{\text{IMF}}(m) m dm}{\int_{m(t)}^{m(t+dt)} f_{\text{IMF}}(m) dm}. \quad (8)$$

Note that the value of the normalisation constant A in Eq. (3) does not matter.

The relation between K-band magnitude and mass was constructed in paper II from the points on each of the Padova isochrones when stars reach their peak brightness in the K-band. The relation was monotonic for AGB stars and RSGs; in the mass regime $0.7 < \log(M/M_\odot) < 1.2$ – 1.3 the Padova isochrones suggest an excursion towards fainter K-band magnitudes. The stellar evolution models for these super-AGB stars are truncated. We compared two different approaches to deal with this: [1] interpolation of the M – K relation through the mass range of super-AGB stars, or [2] accepting the jump to fainter magnitudes from AGB to super-AGB stars. The second approach yielded unrealistic results for the SFH while the first approach was credible, so we adopt the interpolation approach here also.

Dusty LPVs suffer from attenuation. While the isochrones of Marigo et al. (2008) include an estimate of the photometric effects of circumstellar dust their values are very uncertain. Instead, we correct for the effects of reddening by tracing the reddened stars, along the reddening vector, back to the point on the isochrone where they would lie in the absence of reddening. As Fig. 1 illustrates, there exist two types of reddening; carbon stars (e.g., at $t = 1$ Gyr, $\log t = 9$) redden very rapidly, resulting in a relatively shallow trajectory in the CMD, whereas oxygen-rich stars (such as low-mass stars at $t = 10$ Gyr, $\log t = 10$) experience a “greyer” type of reddening due to the greater transparency of silicates. We thus obtain reddening-free K-band magnitudes, K_0 , from the relation:

$$K_0 = K + a(1.25 - (J - K)), \quad (9)$$

with $a = 0.52 \text{ mag mag}^{-1}$ for carbon stars and $a = 0.72 \text{ mag mag}^{-1}$ for oxygen-rich stars at $Z = 0.015$, and $a = 0.64 \text{ mag mag}^{-1}$ for carbon stars and $a = 0.78 \text{ mag mag}^{-1}$ for oxygen-rich stars at $Z = 0.008$. The reddening correction will be applied to stars with $(J - K) > 1.5 \text{ mag}$. In the case where no J-band data are available we use a similar reddening correction prescribed as a function of $(H - K)$ colour. In the case neither J- nor H-band data are available we assume a detection limit of $J = 21 \text{ mag}$.

It is therefore important to distinguish between carbon stars and oxygen-rich stars. Unfortunately, such information is not available for the majority of our LPVs in M 33. Instead, we fix the mass range for carbon stars; based on theory and observation in the LMC (Groenewegen & de Jong 1993; van Loon, Marshall & Zijlstra 2005; Girardi & Marigo 2007) we expect at solar and slightly sub-solar metallicity carbon stars to descend from stars in the range $M_{\text{birth}} \sim 1.5$ – $4 M_\odot$ – at low mass the third dredge-up is not strong enough to change the composition of the surface to carbon dominated, while HBB prevents carbon to enrich the surface in higher mass stars. In practice, we first apply the carbon dust correction to all reddened stars; if the derived mass is in the 1.5 – $4 M_\odot$ range then we accept that star as a carbon star, otherwise we re-apply an oxygenous dust correction.

We refer to Paper II for the relations converting the de-reddened K-band magnitude into birth mass, and the birth mass into LPV age, and for the parameterisation of the pulsation duration. To have a meaningful errorbar on the SFR in each age bin, instead of using equal age bins we adjust the sizes of the age bins such that each contain the same number of stars. Despite the rarity of massive LPVs born relatively recently, we are still more able to detect hikes in the star formation rate within the past Gyr than 10 Gyr ago. So a recent “bursty” SFH does not preclude this from having been a feature throughout the assembly of the galaxy.

Finally, in Paper III we realised that the duration of the LPV phase that we detect in our survey is overestimated in the Padova models, resulting in too low values for the SFR. We thus applied a correction to the pulsation duration, and hence to the SFRs that had been derived in Paper II. We will revisit this important issue in detail for the disc and central region in the discussion section.

Furthermore, we stress that, while our method is model dependent, the Padova models are the only models that predict the pulsation behaviour, which is essential information for our method to work. We would like to encourage other groups to also predict the pulsation behaviour, to offer another avenue to empirically explore the differences between models. Other models that compute the thermal-pulsing AGB evolution (but, like the Padova models, not for super-AGB stars) include BaSTI (Pietrinferni et al. 2004, 2006). In the Appendix we compare the Mass–Luminosity and Mass–Age relations between the BaSTI and Padova models. The main difference is that the faintest stars, around ~ 17.6 mag) are less massive and older when using the BaSTI models (~ 12 Gyr compared to 10 Gyr when using the Padova models), but the difference is negligible for intermediate-age stars (few Gyr old).

4 RESULTS

4.1 The SFH in the central region of M33

Since we already derived the SFH for the central region of M33 using UIST data in paper II, we first show how this compares to the SFH derived from the WFCAM data.

The distribution over brightness and the present day (birth) mass function of LPVs are shown in Fig. 3. Two peaks can be seen, one at $\log(M/M_\odot) \sim 0.1$ and another at $\log(M/M_\odot) \sim 0.5$. As described in paper IV, the branch of stars brighter than $K_s < 11$ mag was removed from further analysis because these stars are affected by saturation. However, RSGs in M33 are fainter than this, so the derived mass function is not affected.

The SFH of the central square kpc of M33 is shown in Fig. 4, separately as derived from the WFCAM data and from the UIST data. The oldest bin is only shown in part as it extends to (unrealistically) large ages. The only reason it is plotted is to show that, as expected, the star formation rate we estimate for ages exceeding the Hubble time is negligible. Two main epochs of star formation are obvious; a major epoch of formation ≈ 4 –5 Gyr ago ($\log t = 9.6$ –9.7) peaking around 4 Gyr ago at a level ~ 2.5 times as high as during the subsequent couple of Gyr. This is slightly shifted to more recent times compared with the UIST result for

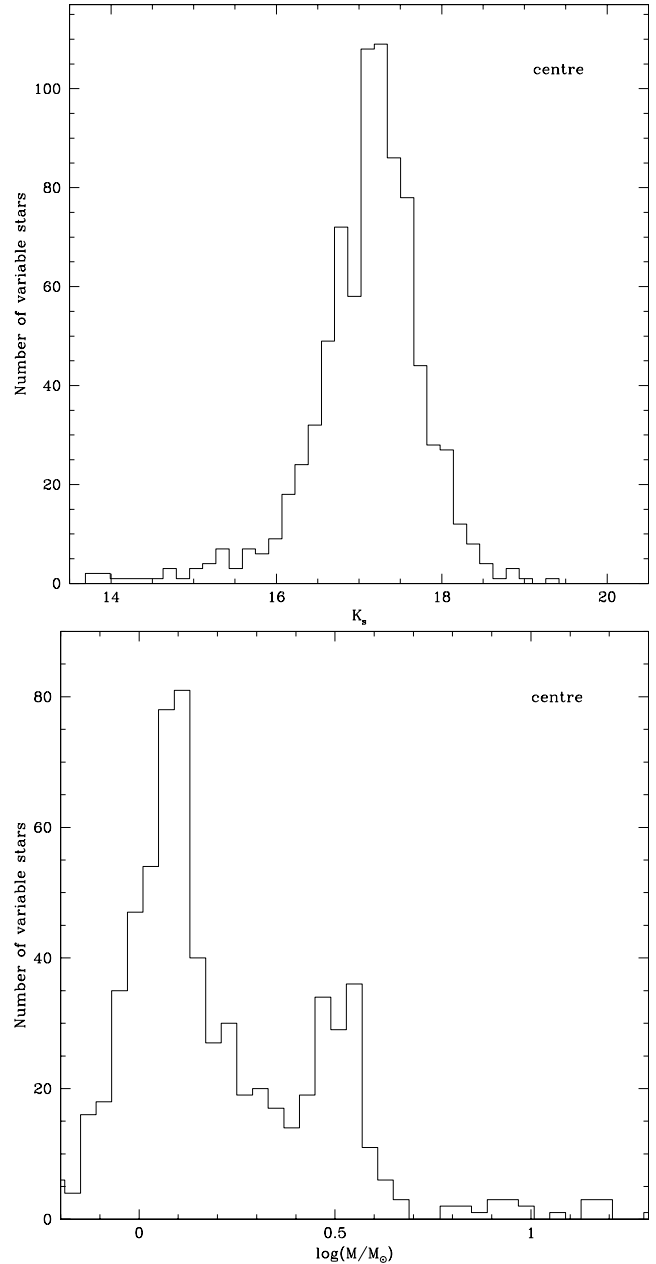


Figure 3. Top: distribution of large-amplitude variable stars, as a function of near-IR brightness in the central square kpc of M33. Bottom: the derived present-day mass function.

which this epoch is ≈ 4 –8 Gyr ago ($\log t = 9.6$ –9.9) with a peak around 6 Gyr ago ($\log t = 9.8$). This could arise from the inferior angular resolution of WFCAM, resulting in incompleteness and blends rendering stars brighter (hence appearing younger) than they really are. The UIST data may be affected too, if less so (the ancient SFR is higher than in the WFCAM data), and hence the peak at 4–6 Gyr may not be real and star formation could well have started – and peaked – earlier. However, this does not change our final conclusion that the SFR in the central regions of M33 has dropped considerably some 4 Gyr ago.

A second epoch of star formation is seen to occur from 300 Myr–20 Myr ago ($\log t = 8.5$ –7.2), in both data sets, with a rate ~ 1.5 times higher than the aforementioned

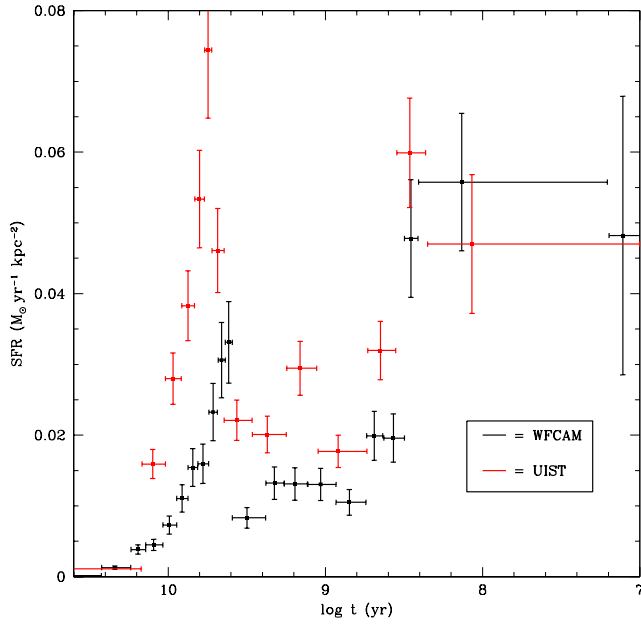


Figure 4. The SFH in the central square kpc of M 33 derived from pulsating AGB stars and RSGs using (*black*;) WFCAM data and (*red*;) UIST data; these rates include a correction of a factor of 7 (WFCAM) or 10 (UIST) – see text.

peak. There is a hint for the SFR to have been decreasing slightly over the course of this more recent epoch, suggesting that something may have happened ~ 300 Myr ago which triggered an enhanced SFR.

4.2 The SFH in the disc of M 33

The WFCAM images reach out to a galactocentric radius of nearly 15 kpc, which includes the pseudo-bulge and most of the disc and spiral arms of M 33. The distribution over brightness and the present day (birth) mass function of LPVs in this larger area are shown in Fig. 5. Again, the mass distribution is dominated by two populations of LPVs; one around $\log(M/M_\odot) = 0.1$ and another around $\log(M/M_\odot) = 0.5$. There are relatively many intermediate-age AGB stars in the disc compared with the central region, and this suggests that the average age of stars in the disc is lower than in the central region.

The SFH across the disc of M 33 is shown in Fig. 6. The double-peaked mass function is again translated into two epochs of enhanced star formation. The old epoch took place ≈ 3 –6 Gyr ago ($\log t = 9.5$ –9.8), peaking ~ 5 Gyr ago ($\log t = 9.7$) at a level almost twice that in the subsequent few Gyr. Barker et al. (2011) showed that the outer disc of M 33 had a major epoch of star formation ~ 2 –4 Gyr ago ($z \sim 0.2$ –0.4 for a standard WMAP Λ CDM cosmology; Dunkley et al. 2009). The offset by one Gyr compared to the timing of this epoch of star formation in the central region (derived from the superior UIST data), suggests that the outer regions of M 33 are younger than the central region. This would confirm the results by Li et al. (2004). This conclusion is, however, controversial since Cioni et al. (2008) suggested the opposite. Because their results were based on photometry with WFCAM, they may have been affected by the crowding in the central regions.

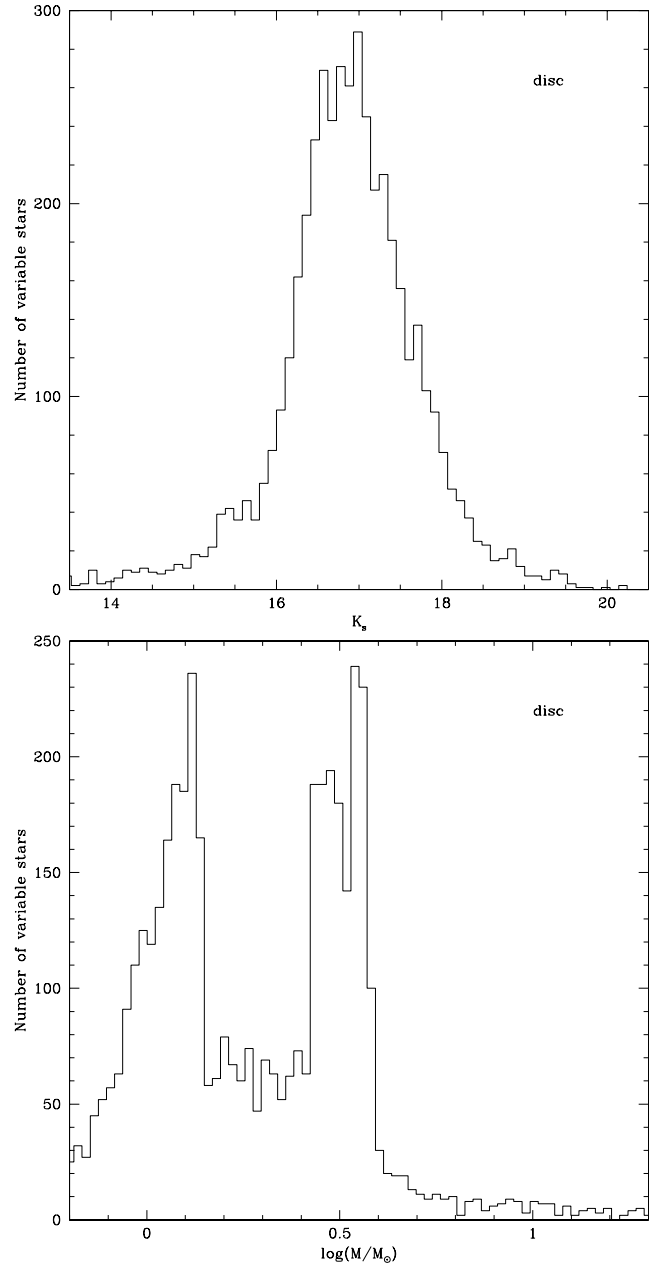


Figure 5. Top: distribution of large-amplitude variable stars, as a function of near-IR brightness in the entire disc of M 33. Bottom: the derived present-day mass function.

The second, recent epoch of enhanced star formation occurred ≈ 200 –300 Myr ago ($\log t = 8.3$ –8.5), reaching a level of almost 4 times that during the earlier epoch of star formation. We caution, though, that this is almost certainly due to the difference in time resolution: the peak of the earlier epoch is an average over ~ 1 Gyr and peaks lasting only ~ 100 Myr may have been much more intense than that. What is beyond doubt, however, is that the more recent peak in SFR is relatively strong compared to the same epoch in the central region of M 33.

While our approach may favour the assignment of the status of carbon star over oxygen-rich star, the SFH results do not change substantially when assuming that all stars are oxygen-rich (see Appendix).

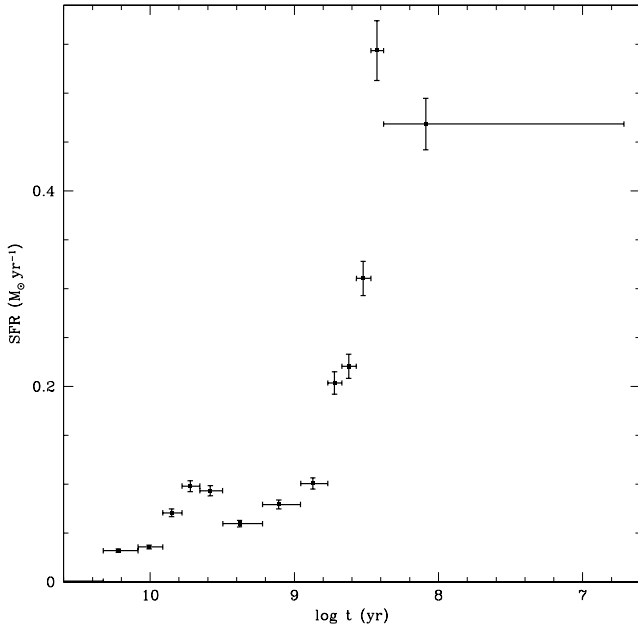


Figure 6. The SFH across the entire disc of M33. A correction factor of 7 has been applied to the SFRs (see text).

4.3 Spatial variation of the SFH across the disc

The variation of SFH as a function of radial distance from the centre of M33 (r) is shown in Fig. 7. Each radius bin contains the same number of variable stars; as a result, the bins grow in size with increasing distance. Two important results become clear immediately; firstly, the old epoch of star formation weakens and then practically disappears as one moves outward through the disc. In the outermost parts of the disc, the star formation rate gradually increases until $t \sim 200$ Myr ($\log t = 8.3$) ago, and then decreases again in more recent times. Secondly, the very recent epoch of star formation is seen across the entire disc at a similar rate, but lower in the very central region. More subtly, star formation at intermediate ages, $t \sim 1$ Gyr ($\log t = 9$) is most pronounced in the most prominent part of the disc, $2 < r < 7$ kpc, but weaker both in the central and the outermost regions.

Gratier et al. (2010) showed that the radial profile of total baryonic mass in M33 displays a double exponential component, with a break around $r \sim 6$ kpc. Within that radius, while the star formation efficiency is relatively constant the SFH shifts to more recent times as one moves outward; this is referred to as the “inside-out” formation scenario. Our analysis (Fig. 7) clearly confirms this scenario for the disc of M33. Fig. 7 also suggests a change in SFH around $r \sim 6$ kpc; beyond that radius, the star formation efficiency decreases (see also Robles-Valdez et al. 2013).

To examine the difference between the disc within $r \leq 6$ kpc and the outer regions at $r > 6$ kpc, the mass functions for these two areas are shown separately in Fig. 8. Apart from an overall drop in stellar content, the outer regions display a conspicuous dearth of intermediate-mass stars (between $\log(M/M_\odot) \sim 0.15$ – 0.4). On the other hand, the outer regions contain more – even in an absolute sense – low-mass, presumably old LPVs ($\log(M/M_\odot) < 0$). In these sparsely populated regions, stars at $\log(M/M_\odot) > 0.4$ could be fore-

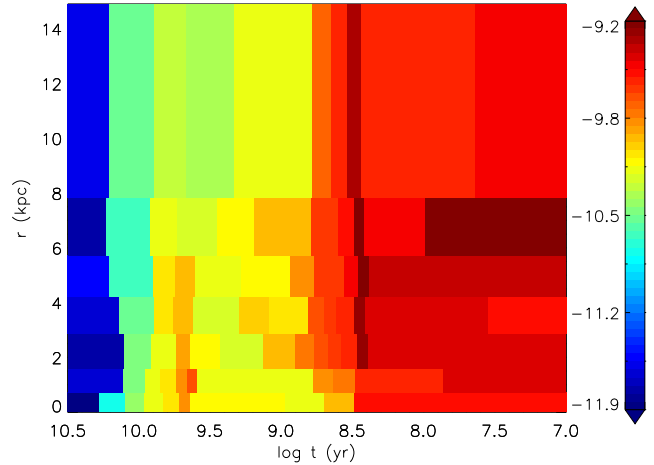


Figure 7. SFH at different radial distance from the centre of M33, in the galaxy (de-projected) plane. The colour bar values are on a logarithmic scale and represent the fraction of the total stellar mass as it formed each year. The inverse of that is the time it takes at that rate, to form all the stars that have ever formed. Each radius bin contains the same number of stars.

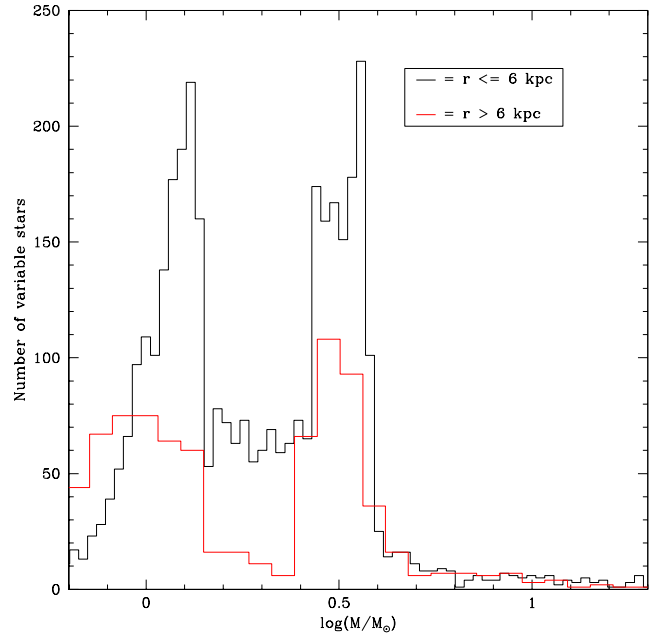


Figure 8. Present-day mass function of large-amplitude variable stars at $r \leq 6$ kpc (black) and at $r > 6$ kpc (red).

ground stars; we provide an estimate of this in Section 4.4. The corresponding SFHs are shown in Fig. 9. Both at $r \leq 6$ kpc and at $r > 6$ kpc there is strong evidence for recent star formation. The old epoch of star formation is present in both areas as well. It is possible that the old stars in the outermost regions were formed further in, but migrated outwards through dynamical relaxation or interaction with spiral arms (Grand, Kawata & Cropper 2012).

4.4 Spatial distribution of stellar populations

We have divided the stellar populations into four different age bins, and plot their spatial distributions in Fig. 10. All

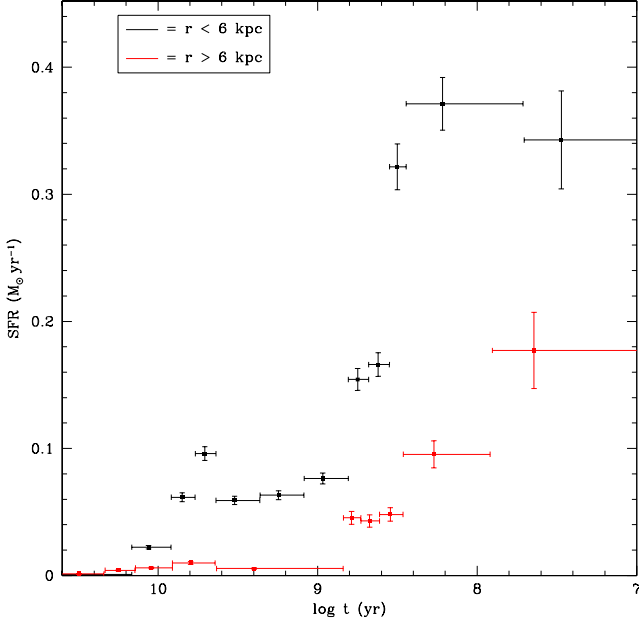


Figure 9. The SFH at $r \leq 6$ kpc (black) and at $r > 6$ kpc (red); these rates include a correction of a factor of 7 (see text) and were derived from near-equally sized areas.

populations are centrally concentrated, but this is especially true for the youngest and – to a lesser extent – the oldest. The intermediate-age populations are distributed more uniformly across the disc. It is interesting to note also the asymmetry in the distributions, with a higher density towards the south. The youngest population exhibits a local overdensity in the North as well, around $23^{\circ}5$ ($1^{\text{h}}34^{\text{m}}$) in right ascension and $+30^{\circ}9$ in declination. The spiral structure is not obvious in these graphs.

To assess the level of contamination by foreground stars we used the TRILEGAL simulation tool (Girardi et al. 2005). We used the default parameters for the structure of the Galaxy, simulating a 0.68 square degree field in the direction of M33 ($l = 133.61^{\circ}$, $b = -31.33^{\circ}$). The region with which we compare this simulation is the area in the galaxy plane that avoided the central $r < 6$ kpc. The result of this comparison is shown in Fig. 11. The variable stars with $0.3 < (J - K_s) < 0.9$ mag experience only a modest level of contamination ($< 8\%$); those with $K_s < 18.2$ mag and $(J - K_s) > 1$ mag are not affected at all. The level of contamination for all sources with $(J - K_s) < 0.87$ mag and those with $(J - K_s) > 0.87$ mag and $K_s > 18.2$ mag is $< 23\%$. These are all upper limits, as most foreground stars would not appear as LPVs.

4.5 SFH and the spiral arm pattern

M33 has two main, inner spiral arms – IN (the northern branch) and IS (the southern branch), indicated by the spiral curves in Fig. 12. These logarithmic arms have a pitch angle of $\theta = 27^{\circ}$ and can be traced out to $r = 3.2$ kpc; they include some of the most prominent HII regions in M33: NGC 604 ($1^{\text{h}}34^{\text{m}}33^{\text{s}}2$, $+30^{\circ}47'06''$), IC 143 ($1^{\text{h}}34^{\text{m}}07^{\text{s}}0$, $+30^{\circ}47'23''$), IC 142 ($1^{\text{h}}33^{\text{m}}55^{\text{s}}8$, $+30^{\circ}45'20''$), NGC 595 ($1^{\text{h}}33^{\text{m}}34^{\text{s}}0$, $+30^{\circ}41'30''$) in IN and IC 137

($1^{\text{h}}33^{\text{m}}29^{\text{s}}3$, $+30^{\circ}31'21''$) in IS. However, the spiral arm pattern of M33 is much more complex, with at least four additional sets of arms that can be traced out to radii of $r \sim 30'$, i.e. > 8 kpc (e.g., Newton 1980; Hagen et al. 2015; Sandage & Humphreys 1980). A sketch of these spirals based on the location of stellar associations is shown in Fig. 12 (Humphreys & Sandage 1978). Most of the arms are covered completely in our survey except for a small part of arms IV N and V N. We note previous attempts were made by Block et al. (2007) to trace the spiral arm structure using near-IR maps of evolved stars; they identified major arcs or carbon stars.

Logarithmic spirals have a form $r = r_0 \exp(b\theta)$ when seen in a face-on view. The pitch angle is defined by $u = \tan^{-1}[b^{-1}(\pi/180) \log e]$ where b is assumed to be constant. Parameters for the ten optical arms in M33 have been given in Sandage & Humphreys (1980), including b and r_0 and the angles (north through east) over which each of the arms exists. To compare the distributions of stars with these logarithmic arm structures, the positions of the stars in the image plane must be deprojected onto the galaxy plane. Then, we can determine the angular distance of stars with respect to each of the arms.

If the spiral arms are the result of a rigidly rotating density wave, then we can express the arc distance, L , in terms of the time since the passage of the density wave:

$$t = \frac{L}{r \times [\Omega_{\text{star}} - \Omega_{\text{pattern}}(r)]} \quad (10)$$

We adopt $\Omega_{\text{pattern}} = 25 \text{ km s}^{-1} \text{ kpc}^{-1}$ from Newton (1980). For the stellar velocity function we adopt (Corbelli & Schneider 1997; in km s^{-1}):

$$v = 101.2 \tanh\left(\frac{r}{7.2}\right) + 8.5 \left[1 + \tanh\left(\frac{r - 32.6}{8.7}\right)\right], \quad (11)$$

where r is the radial distance expressed in arcminutes. This places the co-rotation radius at $r = 3.9$ kpc, beyond which the number of HII regions drops significantly. Obviously, near the co-rotation radius we would not measure any asymmetric lag between stars just born in the density enhancement and older stars dying in the disc behind the wave (diffusion processes would lead to symmetric dispersal). The calculated time lag t of LPVs with respect to arm IIN becomes meaningless within a few hundred pc from the co-rotation radius. We should therefore limit calculations to an area outside the co-rotation radius or set a limit on t ($-0.5 < t < 0.5$ Gyr). The resulting distributions over the time lag, by avoiding an area in the disc within ± 0.3 kpc from the co-rotation radius, is shown in Fig. 13. We also inspected the results we would obtain by placing a limit on t , as well as by adopting a slightly more extended exclusion zone – see Appendix.

We divided our populations of LPVs into five age groups: (1) those formed $t > 10$ Gyr ago; (2) those formed between $5 \text{ Gyr} < t < 10 \text{ Gyr}$ ago during the first epoch of intense star formation; (3) those formed between $1 \text{ Gyr} < t < 5 \text{ Gyr}$ ago, during the period of moderate star formation activity; (4) those formed between $100 \text{ Myr} < t < 1 \text{ Gyr}$ during the recent epoch of enhanced star formation; and (5) massive (super-)AGB stars and RSGs formed $t < 100 \text{ Myr}$ ago. The Southern arms show a concentration near $t = 0$ in all age bins. Arms IS and IIS show the strongest con-

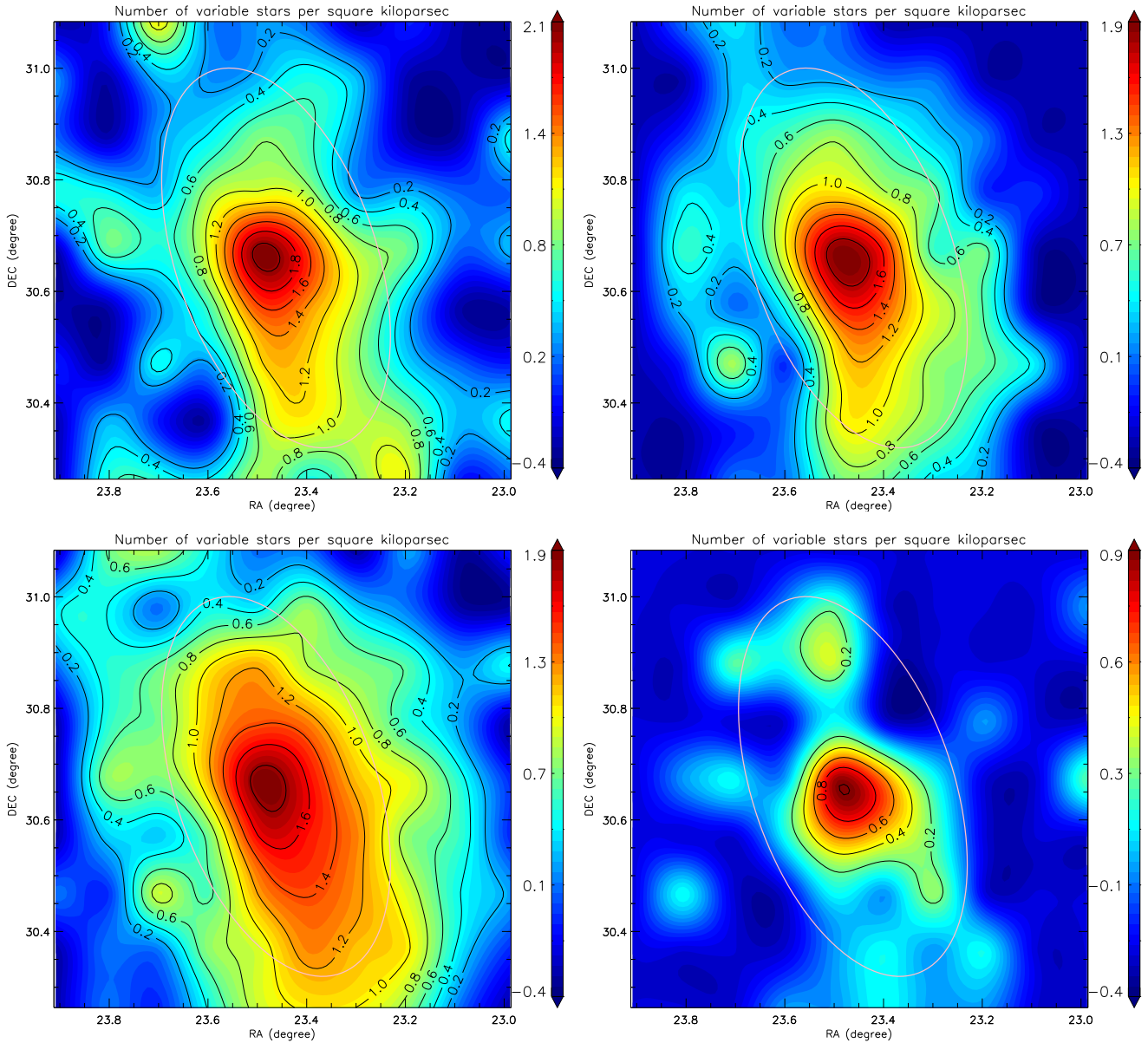


Figure 10. Spatial distribution across M33 of the near-IR LPV populations of (*Top left:*) $t > 5$ Gyr; (*Top right:*) $5 \text{ Gyr} < t < 1 \text{ Gyr}$; (*Bottom Left:*) $1 \text{ Gyr} < t < 100 \text{ Myr}$; (*Bottom right:*) $t < 100 \text{ Myr}$. The units are logarithmic in number of stars per square kpc. The pink ellipse delineates a galactocentric radius of 6 kpc.

centration of massive stars. The Northern arms also show a concentration of stars, in all age bins, near $t = 0$ but not generally at $t = 0$ itself. More surprisingly perhaps, there is no evidence whatsoever for a lag associated with the density wave having passed through the position where we see the stars dying now, or any asymmetry at all.

4.6 Is there any structure?

If spiral arms do not leave a lasting imprint on the distribution of young and intermediate-age stellar populations, one could ask the question whether there is any other structure which evolves with time? To this aim we construct the distribution over nearest-neighbour separations (Fig. 14). The youngest stars ($t < 100 \text{ Myr}$) are indeed more agglomerated

than the older groups of stars. The $100 \text{ Myr} < t < 1 \text{ Gyr}$ population no longer shows any greater agglomeration than still older populations, suggesting that the relaxation time for these structures to dissolve is a few 100 Myr at most. To investigate this in more detail, we divided the group of $100 \text{ Myr} < t < 1 \text{ Gyr}$ stars into two subgroups: those formed between $100 \text{ Myr} < t < 300 \text{ Myr}$ (dotted line in Fig. 14), and those formed between $300 \text{ Myr} < t < 1 \text{ Gyr}$ (dashed line in Fig. 14). The younger of these two groups still shows marginally greater agglomeration, implying a relaxation time of $\sim 200 \text{ Myr}$ (definitely slower than 100 Myr and faster than 300 Myr).

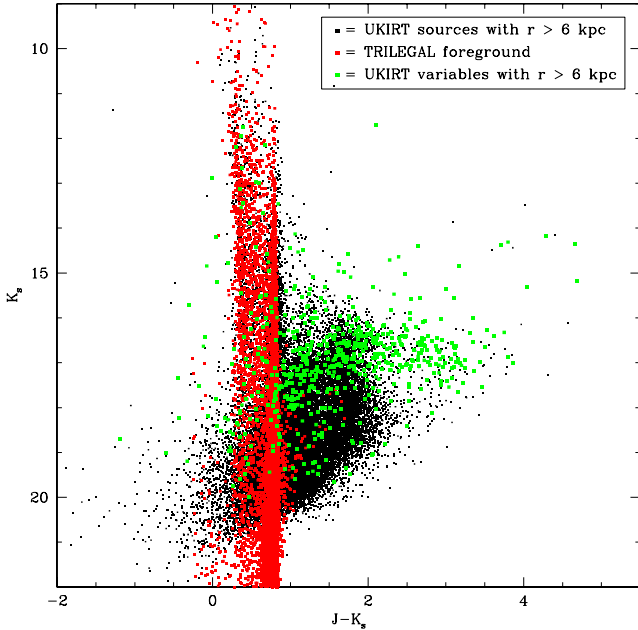


Figure 11. The UKIRT sources (black; variables in green) at $r > 6$ kpc in the galaxy plane. Overplotted in red is a TRILEGAL simulation for the same area of 0.68 square degrees.

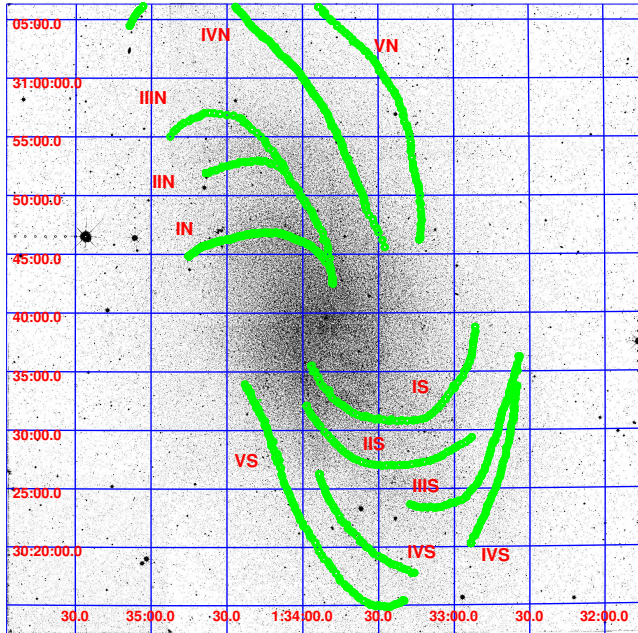


Figure 12. WFCAM K-band mosaic of M33 with the system of five sets of spiral arms marked on it.

4.7 Correlation with ISM density

Because stars form from dense gas, we would expect a correlation between the ISM density and the density of young stars, but not old stars. Using the cold dust density map constructed in Tabatabaei et al. (2014) from *Herschel* Space Observatory and *Spitzer* Space Telescope data of M33, we show in Fig. 15 histograms over ISM dust density, per each age group defined previously. The different age populations exhibit very similar distributions over density, probably be-

cause both stars and gas accumulate in the deepest parts of the potential well (towards the centre, in the disc, and in the spiral arms). The peak ISM dust density for all populations is around $\log \rho(\text{g cm}^{-2}) = -4.75$, which for a gas:dust mass ratio of ~ 200 (Braine et al. 2010) corresponds to ISM densities of $N \sim 10^{21} \text{ cm}^{-2}$ – typical of galaxy discs. The youngest stars ($t < 100$ Myr), however, are slightly biased towards higher ISM dust density, as was to be expected.

5 DISCUSSION

5.1 Correction on pulsation duration

In Paper III we realised that the duration of long period variability is over-estimated by the theoretical Padova models, causing mass loss in excess of the birth mass and an under-estimation of the SFR in our method. While we determined an approximate correction factor ~ 10 (cf. Rezaeikh et al. 2014), this issue needs to be revisited in the light of the new data and larger area of our survey. First, we examine how the SFRs we determined compare with those determined using other methods.

The current or recent SFR in M33 has been estimated from H α emission, or the far-UV or far-IR luminosity by numerous groups (e.g., Hippelein et al. 2003; Engargiola et al. 2003; Heyer et al. 2004; Gardan et al. 2007; Boissier et al. 2007; Verley et al. 2009; Kang et al. 2012). Those SFRs range mostly between $0.02\text{--}0.04 \text{ M}_{\odot} \text{ yr}^{-1} \text{ kpc}^{-2}$ for the central regions of M33. Our new estimate of the current SFR in the central square kpc, which is based on only a small number of RSGs, $\xi = 0.007 \pm 0.003 \text{ M}_{\odot} \text{ yr}^{-1} \text{ kpc}^{-2}$ (Fig. 4) is 3–6 times lower. Verley et al. (2009) estimated the SFR over the past 100 Myr across the disc of M33 to be $\xi = 0.45 \pm 0.10 \text{ M}_{\odot} \text{ yr}^{-1}$. Our estimate for the entire disc of M33 (cf. Fig. 6, multiplied by the area covered) is $\xi = 0.06 \pm 0.04 \text{ M}_{\odot} \text{ yr}^{-1}$, i.e. 7–8 times lower. We thus conclude that our SFRs require multiplication by a factor ~ 7 to be in line with other, independent estimates.

Is there any evidence for this correction factor to depend on mass and/or metallicity? The SFRs for different epochs across the disc of M33 are shown in Fig. 16, assuming the same correction factor of 7 applies to all. If this is correct, then we see that for $t > 4$ Gyr ago, the SFR reaches a maximum value for $r < 2$ kpc and further out it diminishes. At intermediate times, $t \sim 1$ Gyr, the radial profile of the SFR becomes much flatter, and in more recent times the SFR peaks somewhere in the middle of the disc, around $r \sim 3\text{--}5$ kpc (i.e. not far from the co-rotation radius – if there is such a thing as a density wave). How does this compare to independent estimates? Williams et al. (2009) determined the SFH based on *Hubble* Space Telescope images of four fields located at $r = 0.9, 2.5, 4.3$ and 6.1 kpc. The innermost field was characterised by a first epoch of intense star formation at $t \sim 10\text{--}14$ Gyr ago, declining to $\xi = 0.009 \text{ M}_{\odot} \text{ yr}^{-1} \text{ kpc}^{-2}$ before increasing again to $\xi = 0.045 \text{ M}_{\odot} \text{ yr}^{-1} \text{ kpc}^{-2}$ at $t \sim 1\text{--}3$ Gyr ago. The (corrected) SFR at that location derived from our WFCAM data is $\xi \sim 0.01\text{--}0.02 \text{ M}_{\odot} \text{ yr}^{-1} \text{ kpc}^{-2}$ over the past 0.5–6 Gyr. At $t \sim 10$ Gyr our SFR is lower, possibly due to incompleteness at low masses. Around $r = 2.5$ kpc the HST analysis suggested a much steadier SFR without the initial “burst” of star formation,

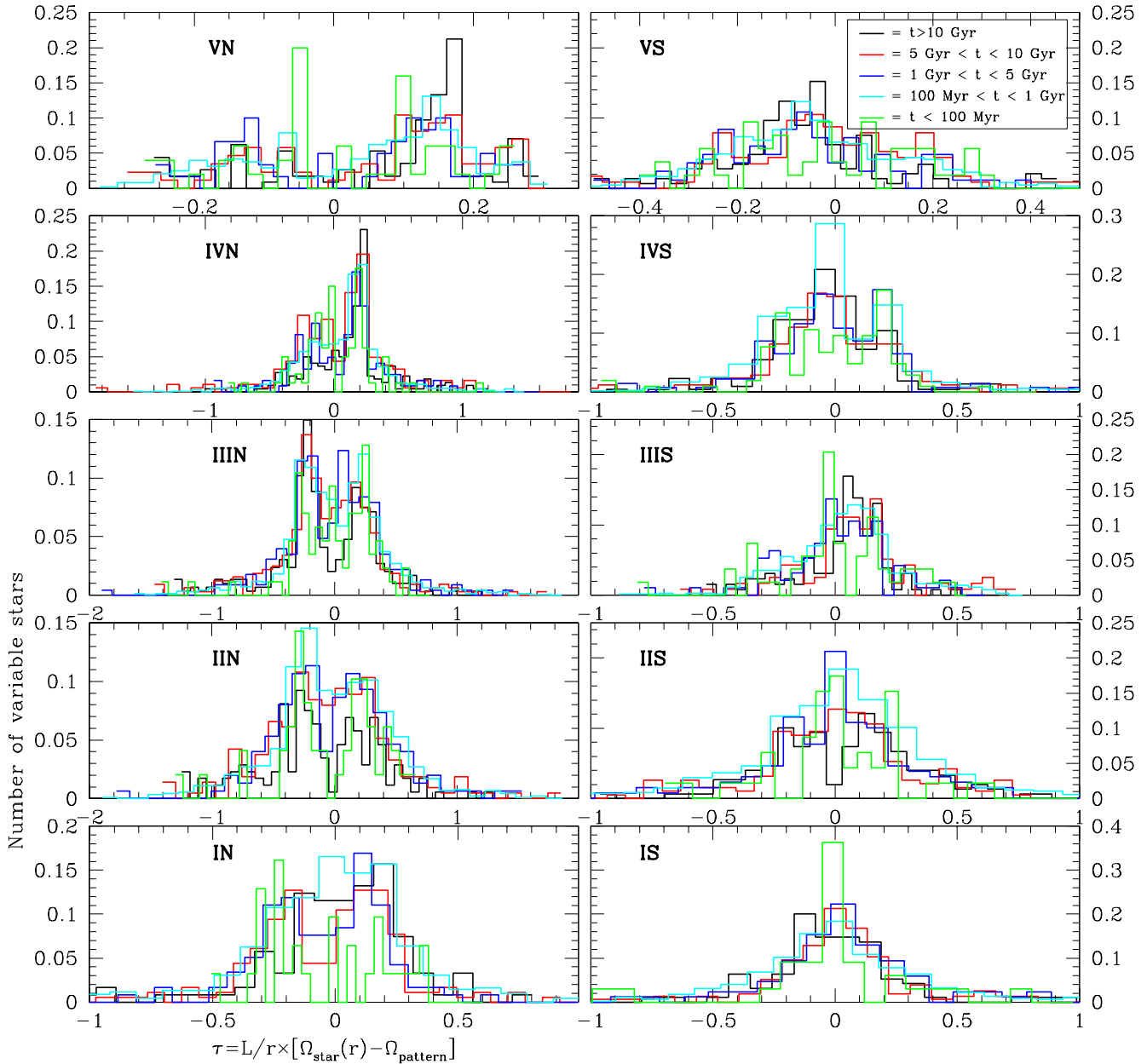


Figure 13. Time lag (in Gyr) of variable stars formed at different times with respect to five sets of spiral arms in the North and South of the disc of M33. The calculations exclude the region around the co-rotation radius, $r = 3.9 \pm 0.3$ kpc.

around $\xi = 0.006 \text{ M}_{\odot} \text{ yr}^{-1} \text{ kpc}^{-2}$. This compares favourably with our estimates at $t = 1$ and 5 Gyr, of $\xi \sim 0.003\text{--}0.18 \text{ M}_{\odot} \text{ yr}^{-1} \text{ kpc}^{-2}$ (Fig. 16). Further out in the disc, Williams et al. (2009) suggest star formation started at a low rate and gradually increased over time. This is very similar to what we see (Figs. 7, 16 and A2). Around $r = 4.3$ kpc, at $t = 2\text{--}8$ Gyr ago Williams et al. (2009) found $\xi \sim 0.003 \text{ M}_{\odot} \text{ yr}^{-1} \text{ kpc}^{-2}$, indistinguishable from our result (Fig. 16); the same is true around $r = 6.1$ kpc. Apart from the oldest stars in the central region, where a larger correction factor might be needed, the consistency with the HST analysis strongly affirms the use of a constant correction factor of 7 for all populations across the disc of M33.

In another study, Barker et al. (2007) observed three fields located at projected radii of $\sim 9\text{--}13$ kpc, SouthEast

of M33's nucleus. They reported a peak in star formation at $t \sim 3\text{--}5$ Gyr ago ($\log t = 9.4\text{--}9.7$) for their fields A1 and A2 with a SFR of $\xi \sim 1.2 \times 10^{-4} \text{ M}_{\odot} \text{ yr}^{-1} \text{ kpc}^{-2}$ and $\xi \sim 2.8 \times 10^{-5} \text{ M}_{\odot} \text{ yr}^{-1} \text{ kpc}^{-2}$, respectively. Apart from that peak, the SFRs are typically 3.5 , 1.8 and $0.8 \times 10^{-5} \text{ M}_{\odot} \text{ yr}^{-1} \text{ kpc}^{-2}$, for their fields A1–3. At $r = 9$ kpc, $t = 3\text{--}5$ Gyr ago, we derive $\xi \sim 1 \times 10^{-4} \text{ M}_{\odot} \text{ yr}^{-1} \text{ kpc}^{-2}$ (corrected; see Fig. A1); further out the SFR drops to $\xi \sim 2 \times 10^{-5} \text{ M}_{\odot} \text{ yr}^{-1} \text{ kpc}^{-2}$. These rates compare very favourably with the results obtained by Barker et al. (2007), vindicating the correction by a factor 7.

The question arises: to what extent is the correction factor due to survey incompleteness? We can address this by looking at the central square kpc of M33. The UIST survey (Paper I) found $N_U = 812$ variable stars; the WFCAM

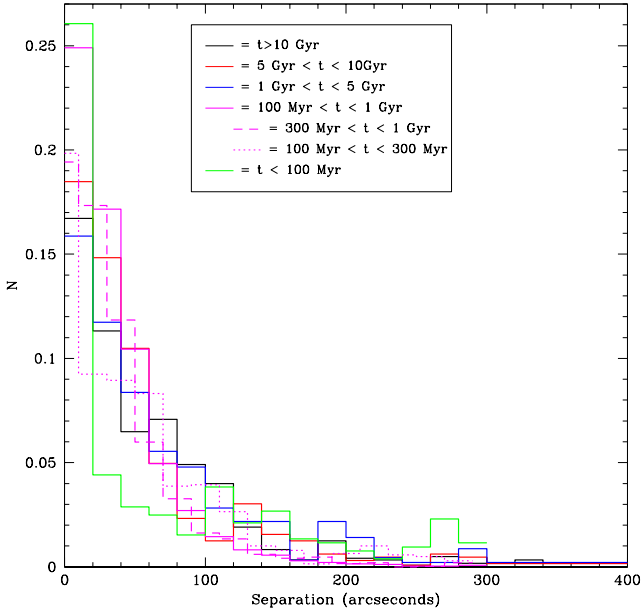


Figure 14. The nearest-neighbour separation distribution of UKIRT variable stars formed at different times. Numbers of stars are normalised to total numbers of stars in each age group.

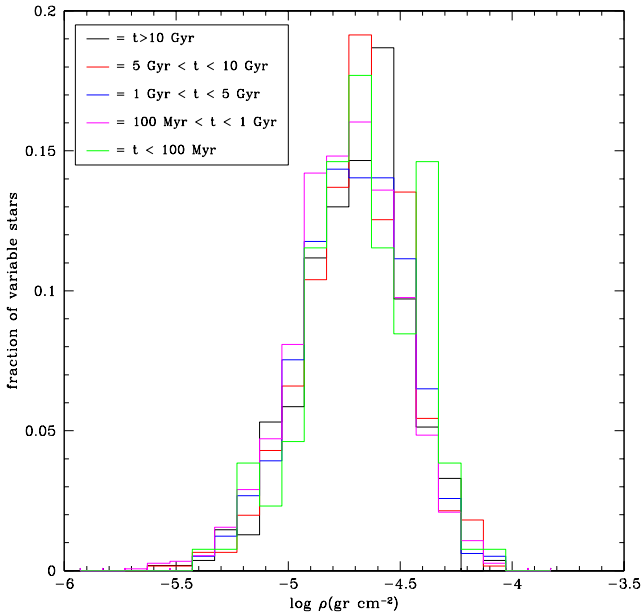


Figure 15. The ISM dust density distribution of UKIRT variable stars formed at different times. Numbers of stars are normalised to total numbers of stars in each age group.

survey (Paper IV) found $N_W = 667$. They had $N_{UW} = 192$ variable stars in common. This already suggests that the UIST survey is no more complete than $N_U/(N_U + N_W - N_{UW}) \times 100 = 63\%$, and likewise the WFCAM survey is no more complete than 52%. This is most likely due to the limited sampling of the lightcurves, as most of the variable stars that are sought have amplitudes that exceed the photometric uncertainties; blending is unlikely to be a major factor as WFCAM recovers 95% of the stars (variable and not variable) detected with the sharper UIST camera. Thus,

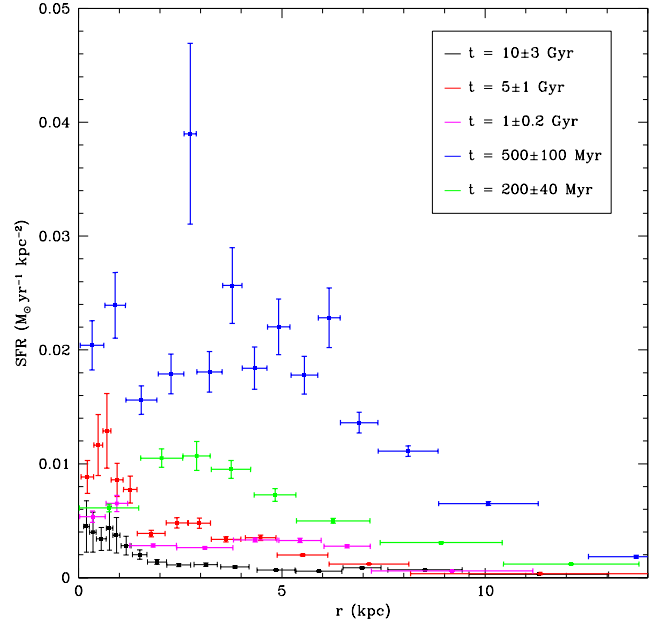


Figure 16. SFR across the disc of M33 at different times. A correction factor of 7 has been applied to the SFRs.

the survey incompleteness of the UIST and WFCAM for the large-amplitude LPVs is likely to be close to 60% and 50%, respectively, leaving another factor 3.5 that we attribute to the over-estimation by the models of the pulsation duration. The latter correction cannot be much smaller than that – and, consequently, the survey incompleteness cannot be much worse than stated above – as the mass-loss catastrophe that first triggered the inquest into the correction factor (Paper III) required a total correction of a factor 10. (We expect that we need to seek to reduce the mass loss estimates by a factor 0.7, for the mass-loss catastrophe to be avoided when adopting a correction to the number of variable stars of a factor 7.)

5.2 Effect of changing the metallicity of older stars on SFH

As time passes, the metallicity of the ISM – and hence that of new generations of stars – changes as a result of nucleosynthesis and feedback from dying stars. Older stars are thus expected to have formed in more metal poor environments than younger stars, though this Age–Metallicity relation may vary spatially within a galaxy. Most of the chemical enrichment occurred > 5 Gyr ago, when a significant fraction of the total stellar mass was put in place (note that chemical enrichment naturally slows down dramatically once the metallicity approaches solar values). While this means that the assumed metallicity in section 4 is quite reliable for young and intermediate-age populations, the oldest populations (> 6 Gyr) might be deficient in metals.

To examine the metallicity effect on the early SFH, we consider the following metallicities: $Z = 0.008, 0.004, 0.0024, 0.0019, 0.0015$ and 0.0012 . The parameterisations of the Mass–Luminosity relation, Mass–Pulsation relation and Mass–Age relation for these different metallicities are provided in the Appendix (see Golshan et al. 2016 for details

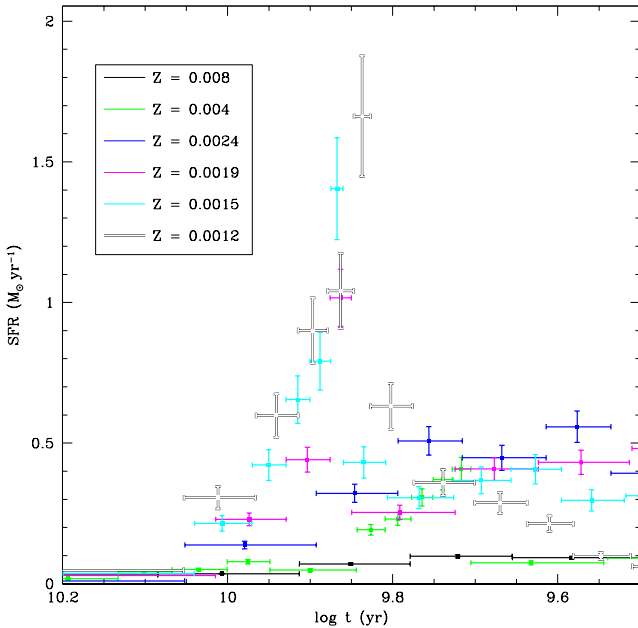


Figure 17. SFH compared for six choices of metallicity.

of the fitting). While the incorporation in our method of an Age–Metallicity relation is non-trivial and beyond the scope of the present work, the resulting SFHs for different – but uniform – values of the metallicity are shown in Fig. 17. Interpretation of this diagram must take notice of what is known about the metallicities of populations of different ages within M33.

Barker et al. (2007) used optical CMDs to determine the SFH and Age–Metallicity relation for three fields at de-projected radii of 9–13 kpc – we consider this the most extreme scenario for any deviation from our assumed metallicity. SFRs peaked ~ 4 Gyr ago in the innermost two fields but > 6 Gyr in the outermost field. Their metallicities are $Z \sim 0.004$ – 0.006 for most of the past ~ 6 Gyr ($\log t < 9.8$), but they were $Z \sim 0.0024$ – 0.003 around $t \sim 10$ Gyr.

For $t < 5$ Gyr ago ($\log t < 9.7$) we see (in Fig. 17) that changing the adopted metallicity from $Z = 0.008$ to $Z = 0.004$ has a negligible effect on the derived SFR. Such change also does not affect the SFRs at the oldest ages ($t > 10$ Gyr), but it does increase the SFRs at $t \sim 6$ Gyr ago by up to a factor three. The change is not very much larger for a metallicity as low as $Z = 0.0024$ or even as low as $Z = 0.0019$. Certainly, while the derived SFRs in the period $6 < t < 10$ Gyr ago ($9.8 < \log t < 10$) would increase by an order of magnitude if the metallicity is as low as $Z = 0.0012$ – 0.0015 , such low metallicities are not appropriate even for the relatively metal-poor outskirts of the M33 disc.

In conclusion, the results we have derived by adopting $Z = 0.008$ across the disc of M33 are robust against reasonable deviations from this value for the metallicity, with a possible modest underestimate of the star formation around $t \sim 6$ – 8 Gyr ago.

5.3 The SFH in M33

In the following, all SFRs are corrected by a factor 7.

The star formation rate has varied between $\sim 0.010 \pm$

0.001 ($\sim 0.012 \pm 0.007$) and 0.060 ± 0.005 (0.052 ± 0.009) $M_{\odot} \text{ yr}^{-1} \text{ kpc}^{-2}$ statistically (systematically) in the central square kiloparsec of M33. The total star formation rate in M33 within a galactocentric radius of 14 kpc has varied between $\sim 0.110 \pm 0.005$ ($\sim 0.174 \pm 0.060$) and $\sim 0.560 \pm 0.028$ ($\sim 0.503 \pm 0.100$) $M_{\odot} \text{ yr}^{-1}$ statistically (systematically). The statistical estimation of SFRs with associated star number statistics (represented by the vertical errorbars) are shown for the central region and the disc in Fig. 4 and Fig. 6, respectively. The systematic estimates of SFRs reflect the variation in SFRs arising from the initial assumptions such as the model we choose, the distance modulus we adopt and the metallicity we adopt. Each of these factors has been investigated carefully in this paper and/or in paper II (see Fig. 10 in paper II for the effect of distance modulus, Fig. 11 in paper II and Fig. 17 in this paper for the metallicity effect and Fig. A4 for the model effect).

We find that the total mass of stars formed in the central square kpc of M33 is $M_{\star} = 2.1 \times 10^8 M_{\odot}$, of which $1.53 \times 10^8 M_{\odot}$ (73%) was formed $t > 4$ Gyr ago ($\log t > 9.6$), but only $1.36 \times 10^7 M_{\odot}$ (6.5%) was formed in the most recent few hundred Myr. These values agree with our previous results based on the UIST data (Paper II). In the disc of M33, we find a total mass of stars $M_{\star} = 1.7 \times 10^9 M_{\odot}$, of which $1.21 \times 10^9 M_{\odot}$ (71%) was formed $t > 3$ Gyr ago ($\log t > 9.5$), but only 2.26×10^8 (13%) was formed in the most recent few hundred Myr. The total mass in stars is at the low end of the range given by Corbelli et al. (2003); we probably missed a significant number of the oldest, lowest-mass stars that do not develop large amplitude pulsation.

Our results suggest that, currently, star formation is more active in the disc than in the central square kpc, and vice versa in the early assembly of M33 – an inside–out formation scenario. Of course, this does not take into account the effect of stellar migration, which may be important for the older populations and most easily discerned in the outskirts where no new stars form (cf. El-Badry et al. 2015; Miranda et al. 2015).

The recent enhancement in the SFR confirms the result of Minniti et al. (1993), who found that the central regions in the disc of M33 experienced enhanced star formation activity over the past 1 Gyr. This may have been caused by interaction with the much more massive Andromeda spiral galaxy, M31 (Richardson et al. 2011). Evidence for interaction comes from the warped shape of the disc (Sandage & Humphreys 1980), and could also have caused the accretion of gas into the central regions necessary to sustain the star formation at the rates observed (Paper III).

Hagen et al. (2015) determined the recent SFH on the basis of UV photometry. The SFR has varied between 0.01 and $1.4 M_{\odot} \text{ yr}^{-1}$ over the past 400 Myr, with the higher values associated with peaks in the SFR around 4 and 10 Myr ago. This is partially due to the better time resolution in recent times, with past such peaks having been smeared out in time to much lower averages. Our estimate of $0.42 M_{\odot} \text{ yr}^{-1}$ over the past 100 Myr is in good agreement with their results.

Kang et al. (2012) constructed a parametrized model to describe the main characteristics of the M33 SFH, assuming a moderate outflow and inside–out formation scenario. The latter agrees with the negative age gradient in the inner disc measured by Williams et al. (2009), as well as our $\xi(t, r)$.

Beyond a certain “break” radius, the older populations regain prominence (Barker et al. 2007). We find that in the central regions the peak in SFR is similar between the old and recent star formation, but this ratio gradually declines as one moves out through the disc of M33, reaching a minimum around $r \sim 8$ kpc where the ancient SFR is only $\sim 10\%$ of that in recent times. At $r > 8$ kpc the stellar population becomes older again. This was also seen for 17 out of 44 face-on galaxies by Ruiz-Lara et al. (2015); they propose that the disc of these systems were formed in their entirety at early times, but that more recent star formation has been quenched from inside-out.

While younger stars ($t < 100$ Myr) are more prevalent in the spiral arms of M33, all stellar populations show a similar concentration towards these arms, with a conspicuous lack of any asymmetry. This means that while stars migrate out of the arms they do not systematically lag behind them. This, in turn, means that the spiral arms do not reflect a density wave potential which has a pattern speed that is notably different from that of the stellar orbital velocities. We conclude that the spiral arms are transient features, in accordance with numerical simulations (e.g., Grand et al. 2012). Junichi et al. (2015) also performed three-dimensional N -body/hydrodynamic simulations and found that the spiral pattern in barred galaxies could change on time scales of 100 Myr, washing out any relation between older stars and spiral arms. This means that grand-design spiral arms in barred galaxies are not stationary, but transient. Our results suggest this is also the case in lower-mass, non-barred spiral galaxies; stars are accumulated temporarily within spiral arms, but over time spans of 100 Myr or more the star formation takes place throughout the disc so stars quickly lose memory of where they were formed.

6 CONCLUSIONS

The photometric catalogue of near-IR variable stars of Paper IV was used to reconstruct the SFH – following the method introduced in Paper II – across the galactic disc of M33 and with respect to its spiral arm pattern. We summarise the main results as follows:

- Most stars in M33, $\approx 71\%$ were formed ~ 5 Gyr ago, i.e. redshift ~ 1 .
- The star formation history of M33 has peaked again more recently, and we detect one such peak ~ 250 Myr ago, lasting ~ 200 Myr and forming $\sim 13\%$ of all stars in M33.
- From the centre outwards through the disc of M33, the early epoch of star formation becomes progressively less pronounced, indicating a youthful disc consistent with an inside-out formation scenario.
- Old stars become more prominent again in the outskirts of M33, at > 8 kpc from the centre, possibly indicating a reduced star formation efficiency in the low density gas in combination with a dynamically relaxed, more extended old stellar population.
- We find that stars of all ages trace some of the spiral arms, but only stars younger than ~ 100 Myr show a greater concentration in the arms; likewise only stars younger than ~ 100 Myr show a greater affinity with high density gas. This indicates that dynamical mixing operates on timescales < 100 Myr.

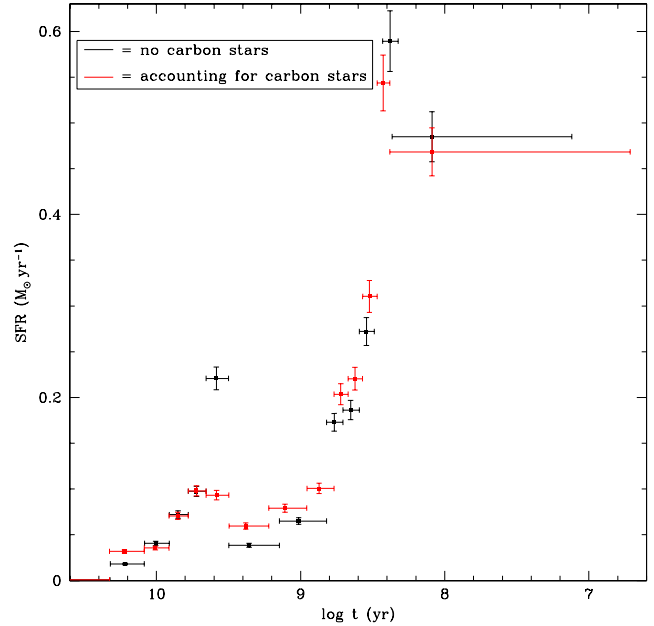


Figure A1. The SFH across the entire disc of M33, assuming all stars are oxygen-rich (black) compared to the SFH we derived assuming intermediate-mass stars will be carbon stars (red); a correction factor of 7 has been applied.

- We determine a survey incompleteness of $\sim 50\%$, and suggest the stellar evolution models we use may have overestimated the lifetimes of the large-amplitude LPV phase by a factor 3 to 4.

APPENDIX A: SUPPLEMENTARY MATERIAL

Here, we show additional diagrams referred to in the text, providing alternative or additional information.

In Fig. A1, we show the SFH assuming all stars are oxygen-rich, i.e. we neglect the fact that stars in a certain mass range will be carbon stars with somewhat different photometric properties. The SFH does not deviate from that in Fig. 6 by a great deal, and our conclusions are therefore not sensitive to the exact manner in which we assign the chemical class to the variable stars.

In Fig. A2, we show how the SFH varies between regions at increasing distance to the centre of M33. This contains similar information to that in Fig. 7, but in a way which facilitates reading off the precise values for the SFR.

In Fig. A3, we show the results of the investigation of the association of stars of different ages with the spiral arms, employing a different (from that in the main body of the paper) exclusion criterion to avoid the singularities arising at the co-rotation radius. The conclusions are unaltered.

In Fig. A4, we compare the Mass–Luminosity relation (in the K-band) for $Z = 0.008$ derived from Padova isochrones with BaSTI isochrones.

In Fig. A5, we compare the Mass–Age relation for $Z = 0.008$ derived from Padova isochrones with BaSTI isochrones.

In Tables A1, A2 and A3, we present parameterisations of the Mass–Luminosity relation, Mass–Age relation and Mass–Pulsation relation derived from the theoretical

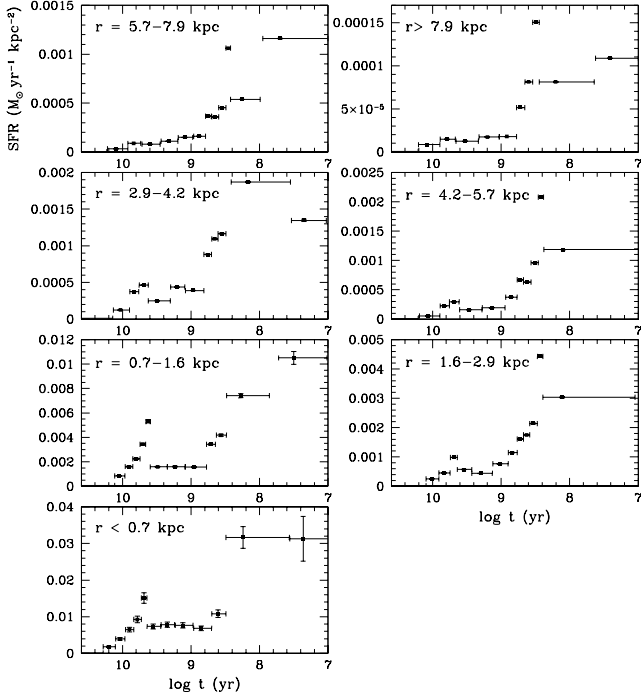


Figure A2. SFH of M33 in different radius bins, in the galaxy plane. A correction factor of 7 has been applied.

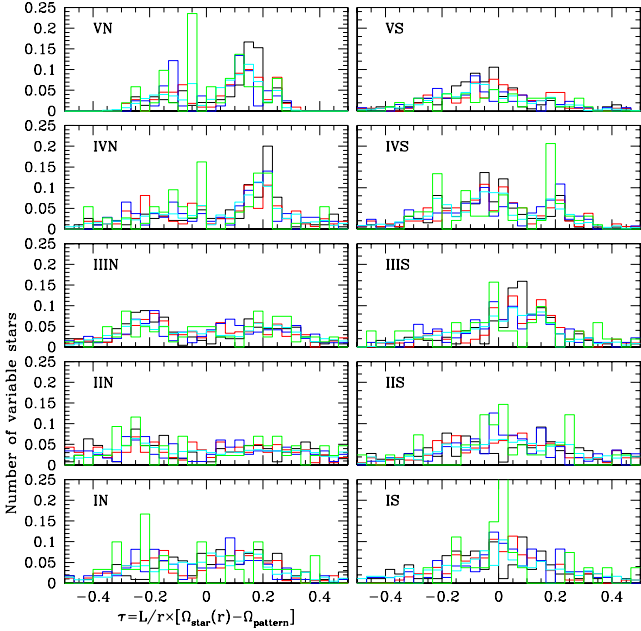


Figure A3. As figure 14, but now the calculations have been limited to time lags of $-0.5 < t < 0.5$.

models of Marigo et al. (2008) and used in our derivation of the SFH in Sections 4 and 5.2.

ACKNOWLEDGMENTS

We thank the staff at UKIRT for their excellent support of this programme. JvL thanks the School of Astronomy at IPM, Tehran, for their hospitality during his visits. We

Table A1. Relation between birth mass and K -band magnitude, log $M = aK + b$, for a distance modulus of $\mu = 0$ mag.

a	b	validity range
$Z = 0.0012$		
-0.447 ± 0.086	-3.502 ± 0.985	$K \leq -11.051$
-0.897 ± 0.084	-8.476 ± 0.904	$-11.051 < K \leq -10.238$
-0.233 ± 0.075	-1.683 ± 0.737	$-10.238 < K \leq -9.426$
-0.085 ± 0.071	-0.286 ± 0.643	$-9.426 < K \leq -8.614$
-0.231 ± 0.062	-1.542 ± 0.503	$-8.614 < K \leq -7.802$
-0.315 ± 0.053	-2.198 ± 0.392	$-7.802 < K \leq -6.989$
-0.080 ± 0.063	-0.553 ± 0.419	$K > -6.989$
$Z = 0.0015$		
-0.447 ± 0.071	-3.477 ± 0.808	$K \leq -11.006$
-0.918 ± 0.066	-8.667 ± 0.698	$-11.006 < K \leq -10.204$
-0.232 ± 0.050	-1.663 ± 0.486	$-10.204 < K \leq -9.401$
-0.094 ± 0.047	-0.362 ± 0.426	$-9.401 < K \leq -8.599$
-0.219 ± 0.041	-1.436 ± 0.329	$-8.599 < K \leq -7.796$
-0.333 ± 0.036	-2.330 ± 0.272	$-7.796 < K \leq -6.994$
-0.062 ± 0.046	-0.432 ± 0.301	$K > -6.994$
$Z = 0.0019$		
-0.508 ± 0.052	-4.152 ± 0.676	$K \leq -10.998$
-0.893 ± 0.048	-8.380 ± 0.649	$-10.998 < K \leq -10.175$
-0.234 ± 0.048	-1.677 ± 0.688	$-10.175 < K \leq -9.383$
-0.095 ± 0.044	-0.362 ± 0.673	$-9.383 < K \leq -8.590$
-0.238 ± 0.038	-1.597 ± 0.606	$-8.590 < K \leq -7.798$
-0.317 ± 0.032	-2.219 ± 0.534	$-7.798 < K \leq -7.000$
-0.076 ± 0.042	-0.524 ± 0.471	$K > -7.000$
$Z = 0.0024$		
-0.475 ± 0.070	-3.777 ± 0.787	$K \leq -10.926$
-0.911 ± 0.061	-8.538 ± 0.645	$-10.926 < K \leq -10.143$
-0.225 ± 0.063	-1.585 ± 0.612	$-10.143 < K \leq -9.359$
-0.098 ± 0.060	-0.393 ± 0.536	$-9.359 < K \leq -8.576$
-0.253 ± 0.051	-1.722 ± 0.412	$-8.576 < K \leq -7.792$
-0.256 ± 0.042	-1.743 ± 0.308	$-7.792 < K \leq -7.009$
-0.147 ± 0.057	-0.985 ± 0.382	$K > -7.009$
$Z = 0.004$		
-0.544 ± 0.087	-4.621 ± 0.971	$K \leq -10.819$
-0.803 ± 0.074	-7.423 ± 0.771	$-10.819 < K \leq -10.083$
-0.215 ± 0.073	-1.492 ± 0.707	$-10.083 < K \leq -9.347$
-0.076 ± 0.070	-0.194 ± 0.634	$-9.347 < K \leq -8.610$
-0.321 ± 0.061	-2.304 ± 0.501	$-8.610 < K \leq -7.874$
-0.213 ± 0.052	-1.452 ± 0.396	$-7.874 < K \leq -7.138$
-0.142 ± 0.071	-0.949 ± 0.489	$K > -7.138$
$Z = 0.008$		
-0.840	-8.076	$K \leq -11.168$
-0.589	-5.275	$-11.168 < K \leq -10.113$
-0.188 ± 0.028	-1.216 ± 0.043	$-10.113 < K \leq -9.600$
-0.142 ± 0.027	-0.778 ± 0.041	$-9.600 < K \leq -9.087$
-0.188 ± 0.022	-1.194 ± 0.036	$-9.087 < K \leq -8.573$
-0.501 ± 0.016	-4.291 ± 0.024	$-8.573 < K \leq -8.060$
-0.248 ± 0.018	-1.840 ± 0.026	$-8.060 < K \leq -7.547$
-0.128 ± 0.025	-0.930 ± 0.035	$K > -7.547$

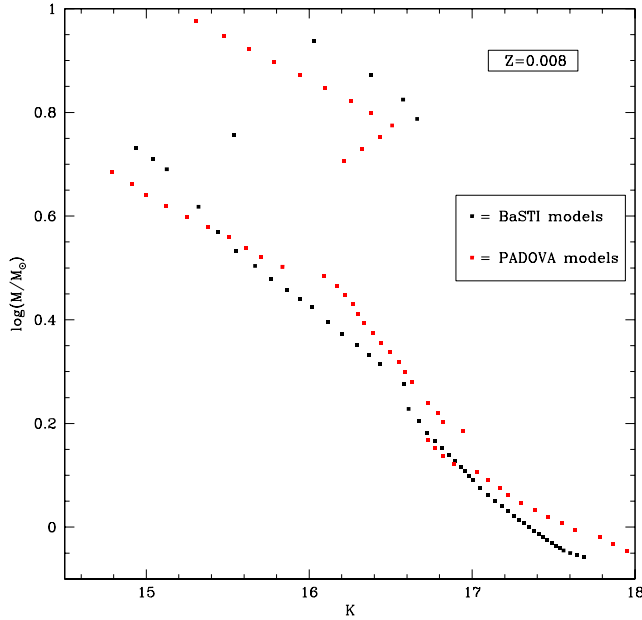


Figure A4. Mass–Luminosity relation (in the K-band) for $Z = 0.008$ and a distance modulus of $\mu = 24.9$ mag derived from the BaSTI isochrones (in black) and Padova isochrones (in red).

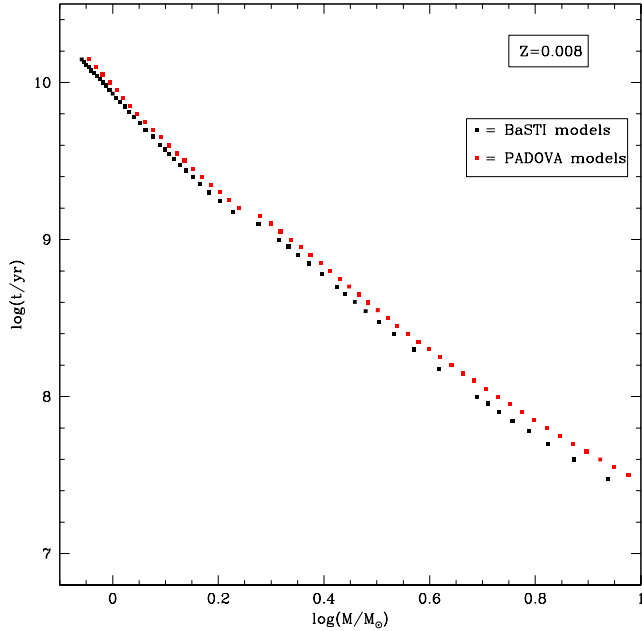


Figure A5. (Birth) Mass–Age relation of AGB stars for $Z = 0.008$ derived from the BaSTI isochrones (in black) and Padova isochrones (in red).

are grateful for financial support by The Leverhulme Trust under grant No. RF/4/RFG/2007/0297, by the Royal Astronomical Society, and by the Royal Society under grant No. IE130487. FST acknowledges financial support from the Spanish Ministry of Economy and Competitiveness (MINECO) under grant number AYA2013-41243-P. Finally, we thank the referee for her/his constructive report which prompted us to improve the manuscript. This work has made use of BaSTI web tools.

Table A1 – *continued*

$Z = 0.015$		
–2.198	–23.425	$K \leq -11.267$
–0.535	–4.696	$-11.267 < K \leq -10.046$
-0.213 ± 0.027	-1.459 ± 0.040	$-10.046 < K \leq -9.553$
-0.088 ± 0.018	-0.267 ± 0.023	$-9.553 < K \leq -9.060$
-0.222 ± 0.021	-1.472 ± 0.024	$-9.060 < K \leq -8.568$
-0.582 ± 0.012	-4.554 ± 0.014	$-8.568 < K \leq -8.075$
-0.147 ± 0.013	-1.040 ± 0.016	$-8.075 < K \leq -7.582$
-0.173 ± 0.022	-1.247 ± 0.032	$K > -7.582$

REFERENCES

- Barker M. K., Sarajedini A., Geisler D., Harding P., Schommer R., 2007, *AJ*, 133, 1138
- Barker M. K., Ferguson A. M. N., Cole A. A., Ibata R., Irwin M., Lewis G. F., Smecker-Hane T. A., Tanvir N. R., 2011, *MNRAS*, 410, 504
- Bertelli G., Mateo M., Chiosi C., Bressan A., 1992, *ApJ*, 388, 400
- Bigiel F., Leroy A., Walter F., Brinks E., de Block W. J. G., Madore B., Thornley M. D., 2008, *AJ*, 136, 2846
- Blanton M. R., et al., 2003, *ApJ*, 594, 186
- Block D. L., et al., 2007, *A&A*, 471, 467
- Boissier S., et al., 2007, *ApJS*, 173, 524
- Bonanos A. Z., et al., 2006, *ApJ*, 652, 313
- Braine J., et al., 2010, *A&A*, 518, L69
- Brook C. B., Kawata D., Gibson B. K., Freeman K. C., 2004, *ApJ*, 612, 894
- Brooks A. M., Governato F., Quinn T., Brook C. B., Wadsley J., 2009, *ApJ*, 694, 396
- Brown T. M., Ferguson H. C., Smith E., Kimble R. A., Sweigart A. V., Renzini A., Rich M. R., VandenBerg D. A., 2003, *ApJ*, 592, L17
- Chang R. X., Hou J. L., Shen S. Y., Shu C. G., 2010, *ApJ*, 722, 380
- Cioni M.-R. L., Irwin M., Ferguson A. M. N., McConnachie A., Conn B. C., Huxor A., Ibata R., Lewis G., Tanvir N., 2008, *A&A*, 487, 13
- Cole A. A., Tolstoy E., Gallagher J. S. III., Smecker-Hane T. A., 2005, *AJ*, 129, 1465
- Corbelli E., 2003, *MNRAS*, 342, 199
- Corbelli E., Schneider S., 1997, *ApJ*, 479, 244
- Doherty C. L., Gil-Pons P., Siess L., Lattanzio J. C., Lau H. H. B., 2015, *MNRAS*, 446, 2599
- Dohm-Palmer R. C., et al., 1997, *AJ*, 114, 2527
- Dunkley J., et al., 2009, *ApJS*, 180, 306
- Eggen O. J., Lynden-Bell D., Sandage A. R., 1962, *ApJ*, 136, 748
- El-Badry K., Wetzel A., Geha M., Hopkins P. F., Kereš D., Chan T. K., Faucher-Giguère C.-A., 2015, *arXiv:1512.01235*
- Engargiola G., Plambeck R. L., Rosolowsky E., Blitz L., 2003, *ApJS*, 149, 343
- Fall S. M., Efsthathiou G., 1980, *MNRAS*, 193, 189
- Ferguson A. M. N., Irwin M. J., Ibata R. A., Lewis G. F., Tanvir N. R., 2002, *AJ*, 124, 1452
- Freeman K. C., Bland-Hawthorn J., 2002, *ARA&A*, 40, 487
- Gallart C., Freedman W. L., Aparicio A., Bertelli G., Chiosi C., 1999, *AJ*, 118, 2245
- Gardan E., Braine J., Schuster K. F., Brouillet N., Sievers A., 2007, *A&A*, 473, 91
- Girardi L., Marigo P., 2007, *A&A*, 462, 237
- Girardi L., Groenewegen M. A. T., Hatziminaoglou E., da Costa L., 2005, *A&A*, 436, 895
- Golshan R. H., Javadi A., van Loon J. Th., Khosroshahi H., Saremi E., 2016, *MNRAS*, Submitted
- Grand R. J. J., Kawata D., Cropper M., 2012, *MNRAS*, 421, 1529

- Gratier P., et al., 2010, *A&A*, 522, A3
- Groenewegen M. A. T., de Jong T., 1993, *A&A*, 267, 410
- Hagen L. M. Z., Siegel M. H., Gronwall C. A., Hoversten E. A., Vargas A., Immler S., 2015, arXiv:1504.6635
- Harbeck D., et al., 2001, *AJ*, 122, 3092
- Harris J., Zaritsky D., 2004, *AJ*, 127, 153
- Heger A., Woosley S. E., Spruit H. C., 2005, *ApJ*, 626, 350
- Heyer M. H., Corbelli E., Schneider S. E., Young J. S., 2004, *ApJ*, 602, 723
- Hippelein H., Haas M., Tuffs R. J., Lemke D., Stickel M., Klaas U., Volk H. J., 2003, *A&A*, 407, 137
- Holtzman J. A., et al., 1999, *AJ*, 118, 2262
- Humphreys R., Sandage A., 1978, *Ann.Rep.Carnegie Inst.*, 77, 180
- Iben I. Jr., Renzini A., 1983, *ARA&A*, 21, 271
- Ita Y., et al., 2004a, *MNRAS*, 347, 720
- Ita Y., et al., 2004b, *MNRAS*, 353, 705
- Javadi A., van Loon J. Th., Mirtorabi M. T., 2011a, *MNRAS*, 411, 263 (Paper I)
- Javadi A., van Loon J. Th., Mirtorabi M. T., 2011b, *MNRAS*, 414, 3394 (Paper II)
- Javadi A., van Loon J. Th., Mirtorabi M. T., 2011c, in: *Why Galaxies Care About AGB Stars II*, eds. F. Kerschbaum, T. Lebzelter & R. F. Wing, ASPC, 445, 497
- Javadi A., van Loon J. Th., Khosroshahi H., Mirtorabi M. T., 2013, *MNRAS*, 432, 2824 (Paper III)
- Javadi A., van Loon J. Th., Khosroshahi H., Mirtorabi M. T., 2014, *MNRAS*, 432, 2824 (Paper IV)
- Kang X., Chang R., Yin J., Hou J., Zhang F., Zhang Y., Han Z., 2012, *MNRAS*, 426, 1455
- Kennicutt R. C., 1998, *ApJ*, 498, 541
- Kennicutt R. C., et al., 2007, *ApJ*, 671, 333
- Leroy A. K., Walter F., Brinks E., Bigiel F., de Blok W. J. G., Madore B., Thornley M. D., 2008, *AJ*, 136, 2782
- Li J., et al., 2004, *A&A*, 420, 89
- Licquia T. C., Newman J. A., 2015, *ApJ*, 806, 96
- Magrini L., Stanghellini L., Villaver E., 2009, *ApJ*, 696, 729
- Magrini L., Corbelli E., Galli D., 2007a, *A&A*, 470, 843
- Magrini L., Vlchez J. M., Mampaso A., Corradi R. L. M., Leisy P., 2007a, *A&A*, 470, 865
- Marcon-Uchida M. M., Matteucci F., Costa R. D. D., 2010, *A&A*, 520, A35
- Marigo P., Girardi L., 2007, *A&A*, 469, 239
- Marigo P., Girardi L., Bressan A., Groenewegen M. A. T., Silva L., Granato G. L., 2008, *A&A*, 482, 883
- Martínez-Delgado D., Aparicio A., Gallart C., 1999, *AJ*, 118, 2229
- McMillan P. J., 2011, *MNRAS*, 414, 2446
- Meynet G., Maeder A., 2000, *A&A*, 361, 101
- Miller B. W., Dolphin A. E., Lee M. G., Kim S. C., Hodge P., 2001, *ApJ*, 562, 713
- Miranda M. S., et al., 2015, arXiv:1512.04559
- Mould J., Kristian J., 1986, *ApJ*, 305, 591
- Nakanishi H., Sofue Y., 2015, arXiv:1511.08877
- Newton L., 1980, *MNRAS*, 190, 689
- Olsen K. A. G., 1999, *AJ*, 117, 2244
- Peebles P. J. E., 1984, *ApJ*, 277, 470
- Pietrinferni A., Cassisi S., Salaris M., Castelli F., 2004, *ApJ*, 612, 168
- Pietrinferni A., Cassisi S., Salaris M., Castelli F., 2006, *ApJ*, 642, 797
- Rezaeikh S., Javadi A., Khosroshahi H., van Loon J. Th., 2014, *MNRAS*, 445, 2214
- Richardson J. C., et al., 2011, *ApJ*, 732, 76
- Robertson B., Bullock J. S., Cox T. J., Di Matteo T., Hernquist L., Springel V., Yoshida N., 2006, *ApJ*, 645, 986
- Robles-Valdez F., Carigi L., Peimbert M., 2013, *MNRAS*, 429, 2351
- Rosolowsky E., Simon J. D., 2008, *ApJ*, 675, 1213
- Ruiz-Lara T., et al., 2015, arXiv:1511.03499
- Sandage A., Humphreys R. M., 1980, *ApJ*, 263, 1
- Sarajedini A., Geisler D., Schommer R., Harding P., 2000, *AJ*, 120, 2437
- Siess L., 2007, *A&A*, 476, 893
- Skillman E. D., Tolstoy E., Cole A. A., Dolphin A. E., Saha A., Gallagher J. S., Dohm-Palmer R. C., Mateo M., 2003, *ApJ*, 596, 253
- Steinmetz M., Navarro J. F., 2002, *New Astronomy*, 7, 155
- Stewart K. R., Bullock J. S., Wechsler R. H., Maller A. H., 2009, *ApJ*, 702, 307
- Tabatabaei F., et al., 2014, *A&A*, 561, 95
- Tolstoy E., et al., 1998, *AJ*, 116, 1244
- Tosi M., Greggio L., Marconi G., Focardi P., 1991, *AJ*, 102, 951
- U V., Urbaneja M. A., Kudritzki R.-P., Jacobs B. A., Bresolin F., Przybilla N., 2009, *ApJ*, 704, 1120
- van Loon J. Th., Marshall J. R., Zijlstra A. A., 2005, *A&A*, 442, 597
- Verley S., Corbelli E., Giovanardi C., Hunt L. K., 2009, *A&A*, 493, 453
- Williams B. F., Dalcanton J. J., Dolphin A. E., Holtzman J., Sarajedini A., 2009, *ApJ*, 695, L15
- White S. D. M., Rees M. J., 1978, *MNRAS*, 183, 341
- Whitelock P., Feast M., Catchpole R., 1991, *MNRAS*, 248, 276
- Wong T., Blitz L., 2002, *ApJ*, 569, 157
- Wood P. R., 2000, *PASA*, 17, 18
- Wood P. R., Whiteoak J. B., Hughes S. M. G., Bessell M. S., Gardner F. F., Hyland A. R., 1992, *ApJ*, 397, 552
- Wyder T., 2003, *AJ*, 125, 3097
- Zaritsky D., Elston R., Hill J.M., 1989, *AJ*, 97, 97

Table A2. Relation between age and birth mass, $\log t = a \log M + b$.

a	b	validity range
$Z = 0.0012$		
-3.109 ± 0.033	9.842 ± 0.003	$\log M \leq 0.241$
-2.433 ± 0.032	9.678 ± 0.013	$0.241 < \log M \leq 0.555$
-2.043 ± 0.034	9.462 ± 0.024	$0.555 < \log M \leq 0.868$
-1.618 ± 0.039	9.093 ± 0.040	$0.868 < \log M \leq 1.181$
-1.074 ± 0.046	8.451 ± 0.061	$1.181 < \log M \leq 1.495$
-0.833 ± 0.060	8.090 ± 0.097	$\log M > 1.495$
$Z = 0.0015$		
-3.216 ± 0.030	9.860 ± 0.002	$\log M \leq 0.198$
-2.511 ± 0.028	9.720 ± 0.009	$0.198 < \log M \leq 0.465$
-2.238 ± 0.030	9.593 ± 0.018	$0.465 < \log M \leq 0.732$
-1.850 ± 0.033	9.310 ± 0.028	$0.732 < \log M \leq 0.998$
-1.413 ± 0.038	8.873 ± 0.042	$0.998 < \log M \leq 1.265$
-1.063 ± 0.043	8.430 ± 0.060	$1.265 < \log M \leq 1.531$
-0.801 ± 0.054	8.030 ± 0.088	$\log M > 1.531$
$Z = 0.0019$		
-3.221 ± 0.030	9.874 ± 0.002	$\log M \leq 0.200$
-2.511 ± 0.027	9.732 ± 0.009	$0.200 < \log M \leq 0.465$
-2.278 ± 0.029	9.624 ± 0.018	$0.465 < \log M \leq 0.729$
-1.856 ± 0.032	9.317 ± 0.028	$0.729 < \log M \leq 0.993$
-1.442 ± 0.037	8.906 ± 0.041	$0.993 < \log M \leq 1.257$
-1.062 ± 0.043	8.428 ± 0.059	$1.257 < \log M \leq 1.522$
-0.833 ± 0.053	8.078 ± 0.087	$\log M > 1.522$
$Z = 0.0024$		
-3.100 ± 0.035	9.881 ± 0.004	$\log M \leq 0.245$
-2.479 ± 0.033	9.728 ± 0.013	$0.245 < \log M \leq 0.551$
-2.128 ± 0.035	9.535 ± 0.025	$0.551 < \log M \leq 0.857$
-1.649 ± 0.040	9.124 ± 0.040	$0.857 < \log M \leq 1.163$
-1.156 ± 0.047	8.552 ± 0.061	$1.163 < \log M \leq 1.469$
-0.862 ± 0.061	8.119 ± 0.097	$\log M > 1.469$
$Z = 0.004$		
-3.207 ± 0.045	9.904 ± 0.004	$\log M \leq 0.207$
-2.470 ± 0.041	9.751 ± 0.014	$0.207 < \log M \leq 0.465$
-2.398 ± 0.043	9.718 ± 0.025	$0.465 < \log M \leq 0.723$
-1.901 ± 0.047	9.358 ± 0.040	$0.723 < \log M \leq 0.982$
-1.559 ± 0.053	9.023 ± 0.059	$0.982 < \log M \leq 1.240$
-1.083 ± 0.062	8.432 ± 0.084	$1.240 < \log M \leq 1.499$
-0.846 ± 0.078	8.076 ± 0.126	$\log M > 1.499$
$Z = 0.008$		
-3.461 ± 0.008	9.976 ± 0.012	$\log M \leq 0.179$
-2.347 ± 0.007	9.776 ± 0.011	$0.179 < \log M \leq 0.404$
-2.727 ± 0.008	9.930 ± 0.011	$0.404 < \log M \leq 0.628$
-2.154 ± 0.008	9.570 ± 0.014	$0.628 < \log M \leq 0.853$
-1.848 ± 0.009	9.309 ± 0.015	$0.853 < \log M \leq 1.077$
-1.398 ± 0.010	8.825 ± 0.015	$1.077 < \log M \leq 1.302$
-1.134 ± 0.012	8.451 ± 0.017	$1.302 < \log M \leq 1.526$
-0.681 ± 0.015	7.790 ± 0.021	$\log M > 1.526$

Table A2 – continued

$Z = 0.015$		
-3.062 ± 0.007	10.096 ± 0.011	$\log M \leq 0.237$
-2.425 ± 0.007	9.945 ± 0.010	$0.237 < \log M \leq 0.455$
-2.824 ± 0.007	10.127 ± 0.010	$0.455 < \log M \leq 0.674$
-2.316 ± 0.007	9.786 ± 0.011	$0.674 < \log M \leq 0.892$
-1.926 ± 0.008	9.438 ± 0.012	$0.892 < \log M \leq 1.110$
-1.399 ± 0.009	8.853 ± 0.013	$1.110 < \log M \leq 1.328$
-1.180 ± 0.063	8.562 ± 0.067	$1.328 < \log M \leq 1.546$
-0.625 ± 0.013	7.704 ± 0.018	$\log M > 1.546$

Table A3. Relation between the relative pulsation duration and birth mass, $\log(\delta t/t) = D + \Sigma_{i=1}^3 a_i \exp [-(\log M[M_\odot] - b_i)^2 / 2c_i^2]$.

D	i	a	b	c
$Z = 0.0012$				
-5.2	1	1.955	0.173	0.074
	2	2.545	0.545	0.196
	3	2.936	1.539	0.429
$Z = 0.0015$				
-4.9	1	0.850	0.202	0.080
	2	2.265	0.547	0.188
	3	2.748	1.483	0.410
$Z = 0.0019$				
-4.9	1	1.02	0.23	0.056
	2	1.43	0.53	0.129
	3	2.52	1.29	0.576
$Z = 0.0024$				
-4.8	1	1.267	0.222	0.064
	2	1.831	0.529	0.147
	3	2.567	1.302	0.427
$Z = 0.004$				
-5.2	1	1.510	0.229	0.065
	2	1.702	0.508	0.149
	3	3.258	1.320	0.519
$Z = 0.008$				
-3.96	1	2.34	1.281	0.378
	2	1.32	0.460	0.165
	3	0.38	0.145	0.067
$Z = 0.015$				
-3.63	1	2.18	1.238	0.238
	2	1.36	0.514	0.127
	3	0.30	0.228	0.084